

# Sea-ice decline could keep zooplankton deeper for longer

Received: 2 January 2023

Accepted: 24 July 2023

Published online: 28 August 2023

 Check for updates

Hauke Flores<sup>1,11</sup>✉, Gaëlle Veyssière<sup>2,3,11</sup>, Giulia Castellani<sup>1</sup>, Jeremy Wilkinson<sup>2</sup>, Mario Hoppmann<sup>1</sup>, Michael Karcher<sup>1,4</sup>, Lovro Valčić<sup>5</sup>, Astrid Cornils<sup>1</sup>, Maxime Geoffroy<sup>6,7</sup>, Marcel Nicolaus<sup>1</sup>, Barbara Niehoff<sup>1</sup>, Pierre Priou<sup>6,8</sup>, Katrin Schmidt<sup>9</sup> & Julienne Stroeve<sup>3,10</sup>

As Arctic sea ice deteriorates, more light enters the ocean, causing largely unknown effects on the ecosystem. Using an autonomous biophysical observatory, we recorded zooplankton vertical distribution under Arctic sea ice from dusk to dawn of the polar night. Here we show that zooplankton ascend into the under-ice habitat during autumn twilight, following an isolume of  $2.4 \times 10^{-4} \text{ W m}^{-2}$ . We applied this trigger isolume to CMIP6 model outputs accounting for incoming radiation after sunset and before sunrise of the polar night. The models project that, in about three decades, the total time spent by zooplankton in the under-ice habitat could be reduced by up to one month, depending on geographic region. This will impact zooplankton winter survival, the Arctic foodweb, and carbon and nutrient fluxes. These findings highlight the importance of biological processes during the twilight periods for predicting change in high-latitude ecosystems.

The shrinking and thinning sea-ice cover of the Arctic Ocean allows the sunlight to penetrate deeper into the water column and extend the sunlit period in subsurface waters<sup>1–3</sup>. The increased light penetration is already causing profound changes to key ecosystem functions, such as enhanced primary production in the marginal shelf seas, and a shifting phenology of ice algae and phytoplankton blooms<sup>4–7</sup>. The effects of the changing light field on higher trophic levels of the Arctic marine ecosystem, however, are not well understood.

The diel change in light intensity is the primary driver of the largest synchronized movement of organisms on Earth: the diel vertical migration of zooplankton<sup>8</sup> (DVM). Commonly, zooplankton ascend to the surface during the night to feed on plankton and descend to deeper waters during the day to avoid visual predators. In the polar regions, winter-active zooplankton perform a seasonal vertical migration

between greater depths during the polar day and shallow depths during the polar night<sup>9–12</sup>. Besides DVM, polar lipid-rich zooplankton perform an ontogenetic migration, spending the polar night in deep water to overwinter in dormancy<sup>13</sup>. Vertically migrating zooplankton act as an active biological carbon pump (also called a ‘lipid pump’<sup>14</sup>), accounting for 25–132% of the gravitational biological carbon pump driven by sinking particulate organic carbon<sup>15,16</sup>. Furthermore, the foraging success of visual predators, such as fish and marine birds and mammals, depends on the interplay between the timing and depth range of the zooplankton’s vertical migration and light penetration depth<sup>17–19</sup>.

Earlier studies using hydroacoustic measurements demonstrated that the vertical migration of Arctic zooplankton is particularly sensitive to low light intensities, but these studies were unable to resolve the top 20 m of the ice-covered ocean<sup>9,10,20–22</sup>. However, the water layer

<sup>1</sup>Alfred-Wegener-Institut Helmholtz-Zentrum für Polar- und Meeresforschung, Bremerhaven, Germany. <sup>2</sup>British Antarctic Survey, Cambridge, UK.

<sup>3</sup>University College London, Earth Sciences Department, London, UK. <sup>4</sup>O.A.Sys – Ocean Atmosphere Systems GmbH, Hamburg, Germany. <sup>5</sup>Bruncin Observation Systems, Zagreb, Croatia. <sup>6</sup>Centre for Fisheries Ecosystems Research, Fisheries and Marine Institute of Memorial University of Newfoundland and Labrador, St John’s, Newfoundland and Labrador, Canada. <sup>7</sup>Department of Arctic and Marine Biology, The Arctic University of Norway, Tromsø, Norway. <sup>8</sup>Akvaplan-Niva, The Fram Centre, Tromsø, Norway. <sup>9</sup>University of Plymouth, School of Geography, Earth and Environmental Sciences, Plymouth, UK. <sup>10</sup>University of Manitoba, Centre for Earth Observation Science, Winnipeg, Manitoba, Canada. <sup>11</sup>These authors contributed equally: Hauke Flores, Gaëlle Veyssière. ✉e-mail: [Hauke.Flores@awi.de](mailto:Hauke.Flores@awi.de)

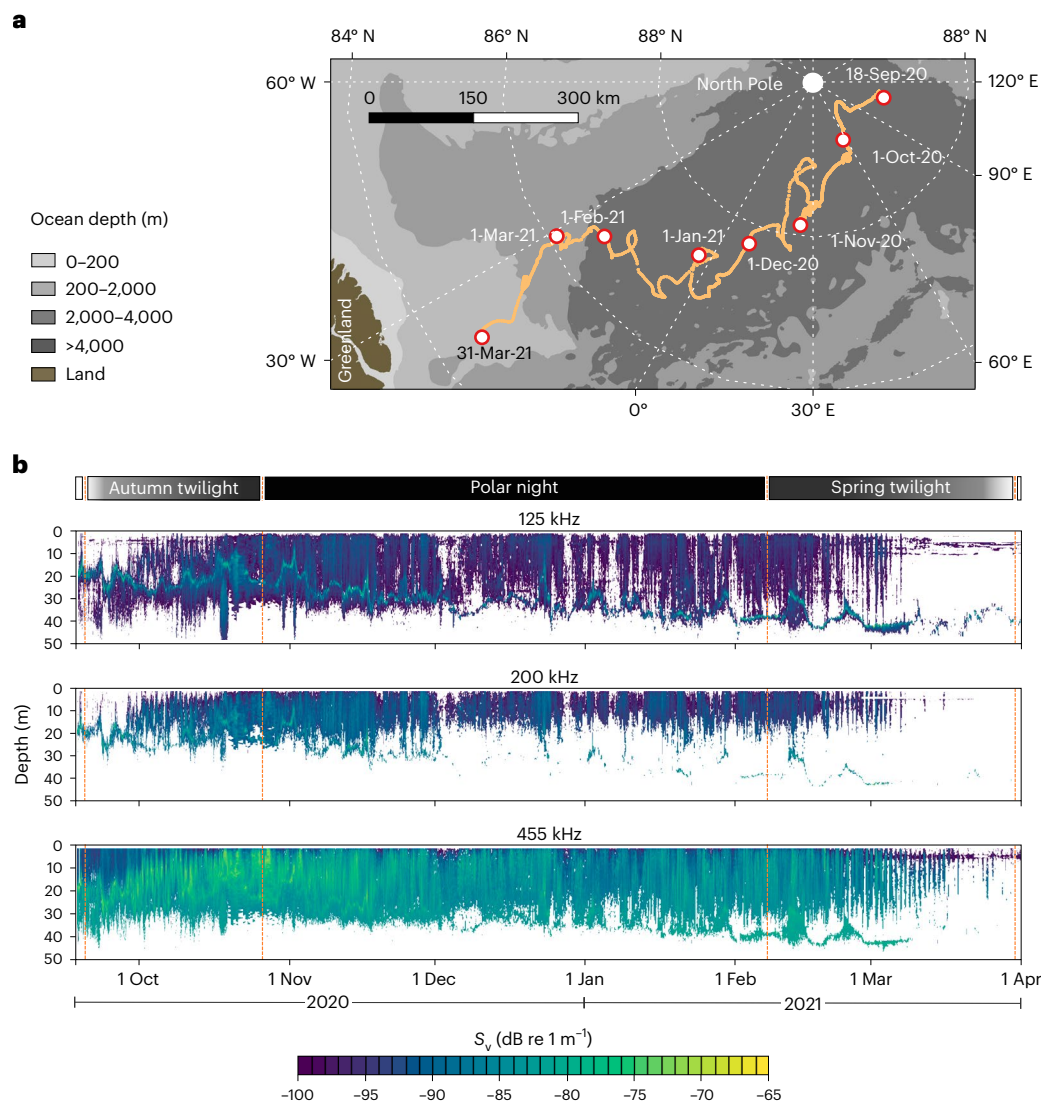


**Fig. 1 | Acoustic backscatter during the drift of the autonomous sea ice observatory.** **a**, Map showing monthly drift positions. Bathymetry: International Bathymetric Chart of the Arctic Ocean (IBCAO) v.4.0 (ref. 55). **b**, Time series plot of mean volume backscattering strength ( $S_v$ ) at 125, 200 and 455 kHz for the

entire observation period. The dashed vertical lines indicate (from left to right) the approximate dates of the first day of the autumn nautical twilight period, the beginning of the polar night, the end of the polar night and the last day of the spring nautical twilight period.

underneath the sea ice, here defined as the ‘under-ice habitat’, is important for zooplankton, because microalgae growing in sea ice (‘ice algae’) may provide critical food supply, particularly during the polar night<sup>23,24</sup>. Increasing light penetration through a thinning sea ice and reduced accumulation of snow may affect the timing of the seasonal migration of zooplankton into and out of the under-ice habitat, and hence the net duration of access to these resources.

Field observations indicate that the vertical migration of zooplankton often follows a trigger level of very low light intensity<sup>22</sup>. This trigger level must be measured under ambient conditions without disturbance by noise or light, both of which are typically emitted by human-operated research platforms<sup>21</sup>. Only then can trigger levels be implemented in coupled biogeochemical sea-ice–ocean models to predict the change in the timing of the seasonal migration into and out of the under-ice habitat based on future light penetration scenarios. In the polar regions, the low light intensities triggering vertical migration occur in the twilight periods during autumn and spring; that is, after sunset and before sunrise. Because both models and satellite products wrongly assume zero incoming radiation once the sun is

below the horizon, an approach considering light penetration during the twilight periods is necessary to realistically model changes in the seasonal migration of zooplankton under sea ice<sup>25</sup>.

To investigate how light intensity controls the vertical migration of zooplankton in the under-ice habitat of the Arctic Ocean, we deployed an ice-tethered, autonomous biophysical observatory drifting across the Central Arctic Ocean (CAO) thousands of kilometres away from any artificial light and noise sources from September 2020 to April 2021. By analysing the data acquired we were able to identify the level of light intensity that triggered vertical migration. To predict likely shifts in the timing of zooplankton vertical migration in the upcoming decades, we applied this trigger level to future light fields derived from experiments of four CMIP6 (Coupled Model Intercomparison Project Phase 6) models with a new approach that made it possible to model the light field under sea ice during the autumn and spring twilight periods. The results allowed us to identify potential changes to the functioning of the high-Arctic ecosystem caused by new vertical migration patterns.

We deployed an autonomous biophysical observatory on sea ice at the end of the MOSAiC drift experiment with RV *Polarstern* in

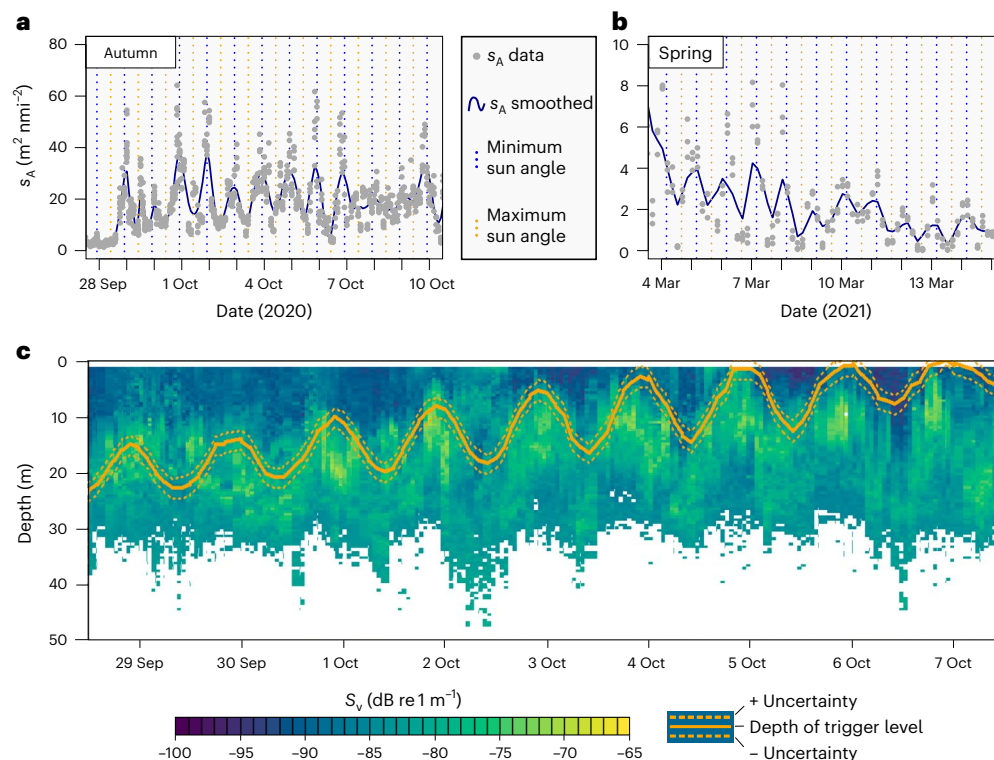


**Fig. 2 | Diel variability of backscatter during the autumn and spring twilight periods. a, b,** Depth-integrated nautical area scattering coefficient ( $s_A$ ) at 455 kHz above the SBM during the autumn (a) and spring (b) twilight periods. Note the different scales of the y-axis in a and b. Relative change in  $s_A$  during the day was

estimated by a loess smoother. **c,** Echogram of the mean volume backscattering strength ( $S_v$ ) at 455 kHz during the 2020 autumn DVM period. The orange trigger level line indicates the depth at which the light intensity under the sea ice equals  $2.4 \times 10^{-4} \text{ W m}^{-2}$ .

September 2020 (*Polarstern* expedition PS122/5)<sup>26,27</sup>. This observatory consisted, among other components, of an Acoustic Zooplankton and Fish Profiler (AZFP) measuring acoustic backscatter at 67, 125, 200 and 455 kHz in the top 50 m of the ocean, a radiation station equipped with hyperspectral light sensors measuring irradiance at the ice underside between 350 and 920 nm (ref. 28), and a CTD (conductivity, temperature, depth) buoy measuring salinity, temperature and pressure at five depth levels (10, 20, 50, 75 and 100 m) (Extended Data Fig. 1 and Supplementary Fig. 1). All data from the observatory were transmitted via the Iridium satellite system. Between the beginning of the measurements on 18 September 2020 close to the North Pole and the end of the study period on 1 April 2021 north of Greenland, the observatory drifted 1,035 km across the CAO (Fig. 1a). After the departure of RV *Polarstern* on 20 September 2020, the observatory was not exposed to external disturbances by noise, artificial light or human activity.

### Observations of zooplankton vertical distribution

We observed changes in the depth distribution of scatterers in relation to the seasonal cycle of solar irradiance at 125, 200 and 455 kHz, whereas there was nearly zero backscatter at 67 kHz. These frequencies are suitable to detect copepods and other mesozooplankton and macrozooplankton as small as 3 mm and make it possible to differentiate the main functional groups of Arctic zooplankton<sup>12,29</sup>. During the end and the beginning of the polar day, the bulk of the backscatter was confined below a subsurface backscatter maximum (SBM) between 20 and 30 m depth, and the water above the SBM was virtually void of scatterers (Fig. 1b). Once the sun set and true darkness prevailed close to the surface, however, most of the backscatter was concentrated between the SBM and the ice underside, a water layer we consider as the ‘under-ice habitat’ in the context of this study (Figs. 1 and 2).

During the twilight period following the autumn equinox (22 September 2020), our data showed a 9-day-long period of pronounced DVM across the SBM (Fig. 2). At 455 kHz, the average integrated backscatter ( $s_A$ ) above the SBM varied between about 40  $\text{m}^2 \text{nmi}^{-2}$  at the diel solar minimum and less than 10  $\text{m}^2 \text{nmi}^{-2}$  at the diel solar maximum (Fig. 2a). During the twilight period preceding the spring equinox (22 March 2021), a diel migration pattern was again visible at 455 kHz (Fig. 2b), but very low acoustic backscatter impeded the detection of diel patterns in the higher frequencies (Extended Data Fig. 2).

Multifrequency analysis based on the relative  $s_A$  at 125, 200 and 455 kHz (ref. 12) revealed that copepods dominated the acoustic backscatter (83%) in the 0–50 m surface layer. Larger zooplankton, such as euphausiids or pelagic amphipods, represented 15% of the acoustic signal and were concentrated in the top 5 m under the ice (Extended Data Fig. 3a). Because our hydroacoustic sampling did not include the ice–water interface, ice-associated amphipods probably accounted for a negligible part of the backscatter. Mesozooplankton sampling prior to the deployment of the autonomous observatory confirmed that late copepodite stages and females of *Metridia longa* and *Calanus* spp. dominated the mesozooplankton biovolume in the top 50 m under the sea ice (Extended Data Fig. 3b).

### Trigger level of light intensity

To determine a level of light intensity triggering DVM during the twilight period, we estimated the light intensity when the zooplankton first migrated across the SBM by extrapolating from light measurements at the ice underside into the water column using an exponential decay of light with depth that was measured during the MOSAiC expedition in March and September 2020 (attenuation coefficient  $K_w = 0.14 \pm 0.01 \text{ m}^{-1}$ ). According to this analysis, scatterers crossed the SBM on 28 September 2020, as soon as the light intensity above the SBM



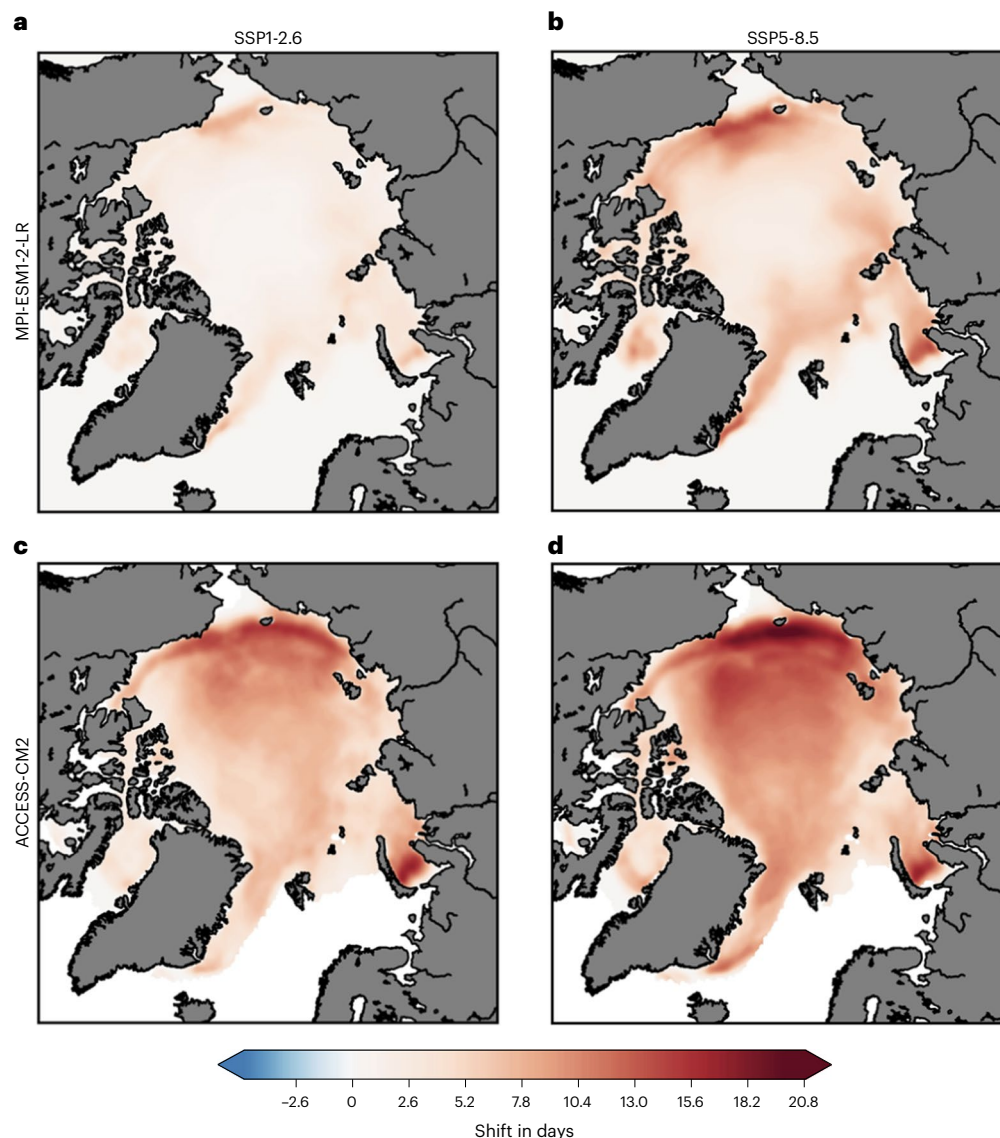


**Fig. 3 | Potential mean shift of autumn DVM onset in mid-21st century compared to present. a–d,** Pan-Arctic maps of the weakest (MPI-ESM1-2-LR) (a,b) and strongest (ACCESS-CM2) (c,d) predicted average shifts of the autumn DVM onset for the SSP1-2.6 (a,c) and SSP5-8.5 (b,d) scenarios, when contrasting 2045–2054 with the baseline in 2015–2024.

decreased below  $2.4 \times 10^{-4} \text{ W m}^{-2}$ . Based on the standard deviation of  $K_w$ , this value was associated with an uncertainty of  $\pm 0.65 \times 10^{-4} \text{ W m}^{-2}$ . Once this trigger isolume reached the ice underside on 7 October 2020, high backscatter remained distributed in the under-ice habitat until the spring twilight period. Between these dates, the scatterers timed their vertical migration to stay below the trigger isolume, performing DVM while following the movement of the isolume up and down with the diel light cycle (Fig. 2c). Accordingly, mean volume backscatter strength ( $S_v$ ) at all three analysed frequencies was significantly lower above the trigger isolume than below it during the DVM period (paired  $t$ -test,  $P < 0.001$  for 125, 200 and 455 KHz, respectively; Methods).

### Future scenarios

As a proxy for the expected mid-21st-century shift in the onset of autumn and spring DVM, we calculated the difference (in days) between the mean date when the trigger isolume reaches 25 m depth in the 10 year period 2015–2024 and the 2045–2054 period. The depth of the trigger isolume was estimated based on light transmitted through sea ice and snow calculated from four different CMIP6 models. Each model

was computed for the two scenarios SSP1-2.6 and SSP5-8.5, respectively, which consider different levels of greenhouse gas emissions related to socioeconomic growth (Figs. 3 and 4, Table 1 and Supplementary Figs. 4–7). To derive the light levels when the sun was below the horizon, we used twilight downwelling irradiance calculated with the radiation scheme of Spitschan et al.<sup>25</sup>, with corrections for solar angle<sup>30</sup>.

Based on changes in the sea ice and snow cover, the four IPCC models projected a prolonged penetration of the trigger isolume below 25 m depth during the twilight periods, implying marked shifts in the onset of autumn and spring DVM in the surface waters for large parts of the Arctic Ocean. We plotted the projected shifts on continuous pan-Arctic maps (Figs. 3 and 4), and calculated mean shifts ( $\pm$  s.d.) for eight large marine ecosystems (LMEs) defined by the Arctic Council Working Group for the Protection of the Arctic Marine Environment (PAME)<sup>31</sup> (Table 1). Each of the CMIP6 experiments had been repeated several times with identical conditions apart from slightly modified initial conditions, creating an ensemble of experiments (members). The resulting differences between those ensemble members are due to internal variability in the simulated

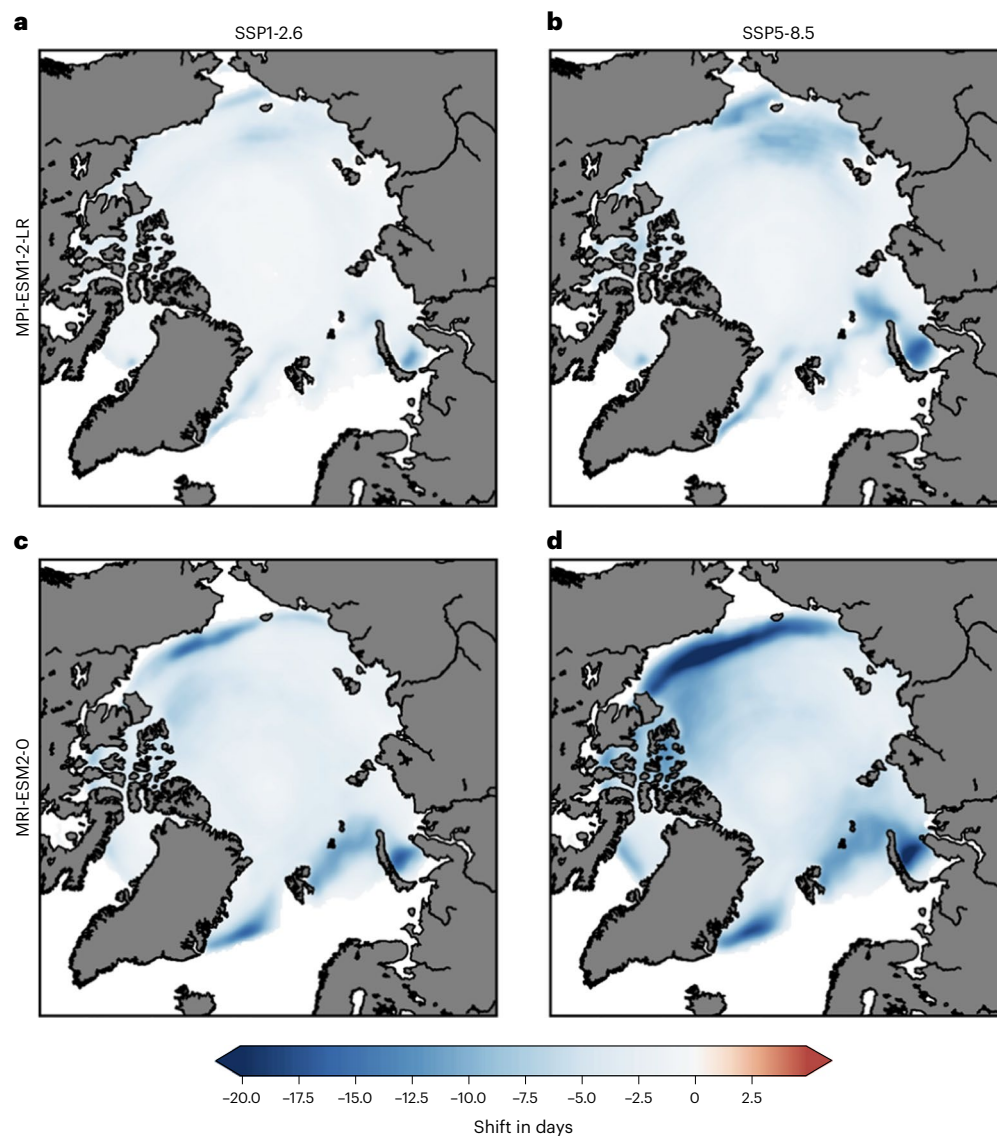


**Fig. 4 | Potential mean shift of spring DVM onset in mid-21st century compared to present.** **a–d**, Pan-Arctic maps of the weakest (MPI-ESM1-2-LR) (**a,b**) and strongest (MRI-ESM2-0) (**c,d**) predicted average shifts of the spring DVM onset for the SSP1-2.6 (**a,c**) and SSP5-8.5 (**b,d**) scenarios, when contrasting 2045–2054 with the baseline in 2015–2024.

coupled systems. In some regions, the simulated internal variability gave rise to a large spread of the model ensembles, reflected in greater standard deviations (Extended Data Fig. 4). We defined the projected mean shifts as ‘robust’ if the ratio of the mean shift to the s.d. was  $\geq 2$  (Table 1). For autumn, the models for SSP1-2.6 predicted robust positive mean shifts between 2 days in the Laptev Sea and 10 days in the Chukchi Sea and the East Siberian Sea, and for SSP5-8.5 between 4 days in the CAO and 14 days in the Beaufort Sea (Table 1). Notably, in the SSP5-8.5 scenario robust positive shifts of 4–9 days were predicted for the CAO, although it was not the most impacted region. Projected robust changes of the depth of the trigger isolume during spring implied a negative shift of the DVM onset to an earlier date between 2 days in the Canadian Archipelago and 9 days in the Chukchi Sea for SSP1-2.6, and between 2 days in the Laptev Sea and 12 days in the Beaufort Sea for SSP5-8.5 (Fig. 4 and Table 1). In spring, standard deviations in those regions with the highest projected shift were also high due to a large ensemble spread, indicating that predictions in these regions were associated with greater uncertainty (Extended Data Fig. 4b).

## Discussion

Our simultaneous observations of zooplankton vertical migration and measured light intensities in the CAO revealed that sufficient light still penetrated the sea ice to control the DVM of zooplankton during the autumn twilight period. This indicates that the timing of the DVM phase marking the seasonal vertical migration of zooplankton at the beginning and the end of the polar night is highly sensitive to predicted increases in light penetration (Fig. 2c)<sup>1</sup>. The trigger level of  $2.4 \times 10^{-4} \text{ W m}^{-2}$  is within the order of magnitude assumed to trigger negative phototaxis in crustacean zooplankton<sup>32</sup>. In a hydro-acoustic study in the ice-free Kongsfjorden, Hobbs et al.<sup>22</sup> found that the DVM of zooplankton followed a trigger level of  $10^{-7} \mu\text{mol photons m}^{-2} \text{ s}^{-1}$ , which had been experimentally determined in female *Calanus* spp. for certain wavelength bands in the blue and green part of the visible spectrum<sup>33</sup>. Converted to photon flux per wavelength band, the portion of energy from our trigger level transmitted within the 530 nm (green) band is  $2.28 \times 10^{-6} \mu\text{mol photons m}^{-2} \text{ s}^{-1}$ , which is within the experimentally determined value range of  $10^{-8}$ – $10^{-6} \text{ photons m}^{-2} \text{ s}^{-1}$  triggering phototactic behaviour in *Calanus* spp. at 525 nm (ref. 33) (Methods).

**Table 1 | Mean shift in onset of DVM in LMEs**

| LME    | SSP1-2.6                |                         |                  |                              | SSP5-8.5                |                         |                   |                              |                  |
|--------|-------------------------|-------------------------|------------------|------------------------------|-------------------------|-------------------------|-------------------|------------------------------|------------------|
|        | ACCESS-CM2 <sup>a</sup> | MRI-ESM2-0 <sup>b</sup> | MPI-ESM1-2-HR    | MPI-ESM1-2-LR <sup>a,b</sup> | ACCESS-CM2 <sup>a</sup> | MRI-ESM2-0 <sup>b</sup> | MPI-ESM1-2-HR     | MPI-ESM1-2-LR <sup>a,b</sup> |                  |
| Autumn | Chukchi Sea             | <b>10.1</b> ±3.6        | <b>6.5</b> ±3.0  | 2.4±2.9                      | 3.6±2.7                 | <b>12.3</b> ±5.0        | 7.9±4.8           | <b>7.4</b> ±3.3              | 6.5±4.8          |
|        | Beaufort Sea            | <b>6.7</b> ±2.8         | <b>9.6</b> ±3.2  | <b>4.3</b> ±2.1              | <b>2.2</b> ±1.1         | <b>9.1</b> ±3.6         | <b>14.0</b> ±5.4  | <b>8.3</b> ±3.1              | <b>5.8</b> ±2.3  |
|        | Canadian Archipelago    | <b>3.5</b> ±1.7         | <b>5.6</b> ±2.4  | 3.2±1.9                      | 1.3±0.9                 | <b>4.4</b> ±1.9         | <b>12.0</b> ±4.4  | <b>7.6</b> ±3.0              | 3.0±2.3          |
|        | Central Arctic Ocean    | <b>6.2</b> ±1.5         | <b>5.6</b> ±1.5  | 1.7±1.5                      | 1.4±0.9                 | <b>8.5</b> ±2.1         | <b>8.1</b> ±3.2   | <b>5.0</b> ±1.7              | <b>3.8</b> ±1.9  |
|        | Barents Sea             | 2.7±1.7                 | 1.2±0.8          | 2.2±1.3                      | 0.5±0.9                 | 2.9±1.9                 | 1.0±0.7           | 3.0±1.9                      | 0.5±1.2          |
|        | Laptev Sea              | <b>5.7</b> ±1.4         | <b>4.8</b> ±1.1  | 2.5±2.0                      | <b>2.3</b> ±1.1         | <b>7.1</b> ±2.1         | <b>5.0</b> ±1.9   | <b>5.4</b> ±1.7              | <b>5.0</b> ±2.2  |
|        | Kara Sea                | <b>7.1</b> ±3.5         | 4.1±2.2          | <b>4.1</b> ±1.7              | 3.1±1.8                 | <b>6.8</b> ±3.4         | 4.7±3.2           | <b>6.6</b> ±1.9              | 5.5±3.7          |
|        | East Siberian Sea       | <b>10.1</b> ±2.5        | <b>6.9</b> ±1.8  | 1.9±1.5                      | 2.2±1.4                 | <b>12.8</b> ±2.9        | <b>7.7</b> ±2.7   | <b>5.2</b> ±2.3              | <b>5.0</b> ±2.3  |
| Spring | Chukchi Sea             | <b>-8.9</b> ±4.0        | -5.5±3.8         | -2.6±2.5                     | -2.6±2.0                | <b>-11.4</b> ±5.7       | -10.1±6.3         | -7.5±4.4                     | -4.7±3.4         |
|        | Beaufort Sea            | <b>-4.6</b> ±1.5        | -6.1±3.1         | -3.1±1.9                     | <b>-2.1</b> ±0.9        | <b>-5.8</b> ±1.9        | <b>-12.0</b> ±5.1 | <b>-4.8</b> ±1.8             | <b>-3.6</b> ±1.5 |
|        | Canadian Archipelago    | -2.9±1.5                | <b>-4.4</b> ±2.1 | -3.2±3.0                     | <b>-1.7</b> ±0.6        | -3.7±1.9                | <b>-8.2</b> ±3.3  | -4.5±2.6                     | -2.8±2.5         |
|        | Central Arctic Ocean    | <b>-2.5</b> ±1.0        | <b>-3.0</b> ±1.1 | -1.1±1.2                     | -1.0±0.7                | <b>-3.3</b> ±1.4        | <b>-5.0</b> ±1.9  | -2.0±1.6                     | -1.7±1.0         |
|        | Barents Sea             | -4.4±3.1                | -6.3±3.8         | -4.3±3.2                     | -0.9±1.6                | -6.7±3.9                | <b>-7.2</b> ±3.8  | -5.9±3.2                     | -1.2±2.3         |
|        | Laptev Sea              | <b>-3.1</b> ±1.4        | <b>-1.9</b> ±0.8 | -0.5±0.9                     | -0.4±0.7                | -2.9±1.6                | <b>-3.2</b> ±1.0  | -1.0±1.2                     | <b>-2.0</b> ±0.9 |
|        | Kara Sea                | -3.4±3.5                | -4.7±4.1         | -2.2±2.9                     | -2.1±2.1                | -4.4±4.5                | -8.6±4.7          | -2.9±2.4                     | -4.7±4.4         |
|        | East Siberian Sea       | <b>-8.2</b> ±2.8        | -2.9±1.5         | -1.4±1.9                     | -2.7±1.9                | <b>-9.8</b> ±3.2        | -5.6±3.7          | -2.8±2.8                     | -5.1±3.0         |

Mean (±s.d.) shift of autumn and spring DVM onset in days for Arctic large marine ecosystems (LMEs)<sup>31</sup> (Supplementary Fig. 2) for all models when contrasting 2045–2054 with the baseline in 2015–2024 under scenarios SSP1-2.6 and SSP5-8.5. Bold numbers indicate ‘robust’ ensemble mean shifts where the ratio of the ensemble mean shift versus the s.d. is ≥2. <sup>a</sup>Models with the weakest and strongest shifts in autumn (Fig. 3) <sup>b</sup>Models with the weakest and strongest shifts in spring (Fig. 4)

DVM is often explained by a trade-off between access to food in the surface layer and predation risk<sup>8</sup>. The darkness of the high-Arctic polar night allows zooplankton to exploit resources from the under-ice habitat without added predation risk. Accordingly, the winter-active copepod *Metridia longa* resides in the surface layer during winter while dwelling at depths >100 m during summer<sup>34,35</sup>. Likewise, parts of the population of *Calanus* spp. remain active in the surface layer during the polar night, whereas the bulk of the population overwinters at greater depths<sup>36</sup>. During the autumn twilight period, chlorophyll-*a* fluorescence measurements by a sensor at the AZFP buoy indicated that some phytoplankton was still available for grazers in the under-ice habitat, but fluorescence steadily declined towards zero by mid-October (Supplementary Fig. 1d). During the polar night, remnant organic matter produced by ice algae may constitute a critical carbon source. Carbon from this ‘sea-ice food bank’ can be transferred into the water column by ice-associated organisms and organic particles released by brine rejection, or through friction between moving ice floes<sup>37–39</sup>. Based on recent studies indicating a year-round importance of ice-algae-produced carbon in polar food webs<sup>24,40,41</sup>, we suggest that this particle rain and its associated microfauna provide low but critical amounts of carbon necessary to satisfy the energy demand of winter-active zooplankton<sup>42,43</sup>. Furthermore, the persistent SBM at 20–30 m depth was probably associated with a strong pycnocline<sup>44</sup> which retained food for zooplankton in the under-ice habitat (Methods and Supplementary Fig. 1e–l). The combination of low predation risk and persistent food availability in and above the SBM probably constituted an energetically positive trade-off for certain winter-active zooplankton species which ceased vertical migration and stayed in the under-ice habitat throughout the polar night.

Future changes in the timing of DVM onset in spring and autumn were inferred from projected changes of the depth of the trigger isolume during the twilight periods based on the output of a subset of four IPCC model ensemble experiments from CMIP6. These models had provided reasonable sensitivity of the sea-ice cover to greenhouse gas forcing<sup>45</sup>. However, the results of the model-based projections

are still subject to various sources of uncertainty, for example, model performance and natural variability<sup>45</sup>. Notably, most of the models tend to underestimate present-day sea-ice thickness and to overestimate present-day sea-ice concentration in the marginal ice zones. This bias is strongest in the regions with the thickest sea ice north of the Canadian and Greenland coast in the Canadian Archipelago region, which were not the areas of focus in this study. Because we limited our study to the effect of changes in sea ice and snow on the light regime for which reliable CMIP6 models exist, we did not consider uncertainty derived from other potential changes that can affect the light regime in the future, for example, a changed albedo. The relations of standard deviations to the ensemble means of each model ensemble (Table 1) provide an indication of the robustness of the respective predicted shifts of the onset of DVM. The standard deviations depend on internal model variability and differ between the models. Robust results across the models show a range of shifts of 4 to 14 days in autumn and –2 to –12 days in spring for SSP5-8.5. We note, however, that within all four models each ensemble member represents a possible reality predicted by its model. Therefore, in some regions, extreme positive and negative shifts outside the standard deviations shown in Table 1 cannot be excluded (Supplementary Tables 2 and 3).

In the period 2045–2055, the peak of the spring phytoplankton bloom is expected to be several weeks earlier than at the present<sup>6</sup>. According to a model study by Tedesco et al.<sup>5</sup>, the spring ice algae bloom north of 80° N will be much more productive (up to 2,500% increase in gross primary production), but it will peak about 6 weeks earlier in the second half of this century compared to the present and will have vanished before the end of summer due to ice melt. Hence, in spite of increased productivity, delayed seasonal upward migration of zooplankton at the onset of the polar night further increase the gap between the peak blooms of phytoplankton and ice algae in early summer and the arrival of zooplankton in the under-ice habitat in autumn. Furthermore, delayed new-ice formation will largely limit the production of new biomass by ice algae in autumn<sup>46</sup>, leading to lower carbon stocks in the ‘sea-ice food bank’ during the polar night (Fig. 5). These effects reduce



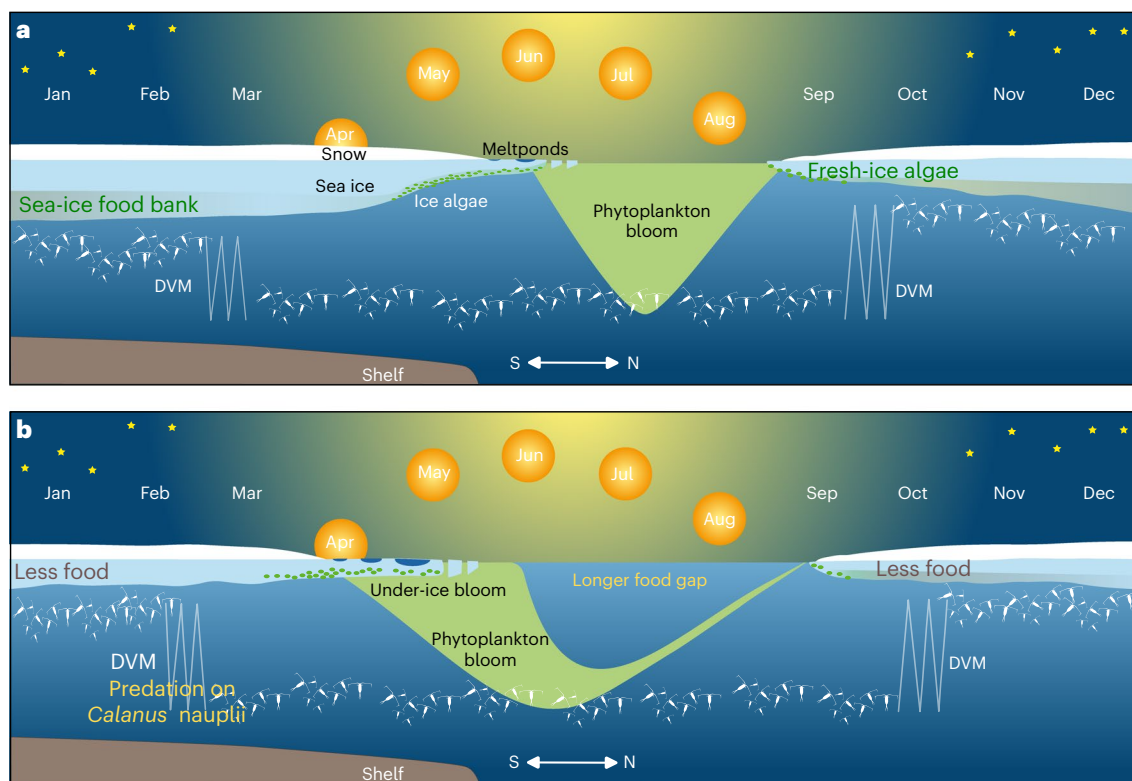


**Fig. 5 | Potential ecological impacts of shifts in the timing of seasonal migrations. a,b** Present (a) and future (b) scenarios showing potential repercussions of negative (spring) and positive (autumn) shifts in the onset of DVM on zooplankton within the surface layer (0–50 m) of the Arctic Ocean, assuming a ‘business-as-usual’ (SSP5-8.5) scenario. The figure shows a schematic annual cycle with the summer in the centre, along a gradient from shelf seas at low latitudes (<80° N, left) to the CAO at high latitudes (>85° N, right). **a**, At present, zooplankton feed on the phytoplankton bloom during polar day. During the polar night, zooplankton dwelling in the under-ice habitat benefit from ice algae-produced carbon stocks, the ‘sea-ice food bank’. The springtime downward migration begins after nauplius larvae of the copepod *C. hyperboreus* have migrated to the surface and developed to copepodites. **b**, In the future, the springtime downward migration may begin so early that

omnivorous zooplankton can prey on the developing *C. hyperboreus* nauplii before they ascend<sup>50</sup>. When they migrate into the under-ice habitat in autumn, zooplankton may have less carbon available due to a shorter productive period of ice algae. At high latitudes, a longer starvation period between the end of the phytoplankton bloom and the delayed migration into the under-ice habitat at the onset of polar night could additionally reduce winter survival of zooplankton. The intensity of the green-brown shading in sea ice symbolizes relative changes in ice algae-produced carbon stocks. The green shading of phytoplankton blooms is not scaled to productivity or biomass. DVM, diel vertical migration during the twilight period. Figure not drawn to scale. This figure is based on scenarios shown in Soreide et al.<sup>56</sup>, Leu et al.<sup>47</sup>, Wassmann and Reigstad<sup>4</sup> and Ardyna and Arrigo<sup>6</sup>, under a Creative Commons License (<https://creativecommons.org/licenses/by/4.0/>).

the survival probability of winter-active zooplankton, because they enter the polar night with lower energy reserves, and will probably find less ice-associated organic matter in the under-ice habitat<sup>4,5,47</sup> (Fig. 5). In addition, earlier downward migration during spring could impact on the ecologically important copepod *Calanus hyperboreus* within its future distribution range. Female *C. hyperboreus* spawn at depth during winter, and the early nauplius larvae rise to the surface, while growing into larger copepodite stages<sup>48,49</sup>. An earlier descent of omnivorous copepods such as *Metridia* spp. can lead to increased predation on *C. hyperboreus* nauplius larvae before they have outgrown the prey size range of *Metridia* spp., compromising the recruitment of *C. hyperboreus*<sup>50</sup> (Fig. 5). Other dynamics may apply in lower latitudes where boreal *Calanus* species may prevail in the future<sup>49</sup>. Ultimately, a reduced energetic trade-off may overall weaken the cue for vertical migration into the under-ice habitat in the future. In the CAO, juvenile and immature polar cod *Boreogadus saida*, the main prey of many Arctic birds and mammals, cover a great part of their energy demand from prey taken in the under-ice habitat<sup>51,52</sup>. Less prey in the under-ice habitat and an overall changing prey field will negatively impact on the survival of young polar cod in the CAO, with cascading effects on higher trophic levels<sup>53</sup>.

The application of a fully autonomous biophysical observatory enabled us to monitor animal behaviour under sea ice during its drift

across the CAO, a task that has so far required immense logistic effort and therefore left considerable knowledge gaps regarding higher trophic levels in the Arctic ecosystem<sup>54</sup>. Similar technology will be important for understanding changes of the future Arctic ecosystem and its management, for example, under the Central Arctic Ocean Fisheries Agreement (CAOFA). By modelling twilight conditions at the beginning and the end of the polar night, our results show that future changes of the under-ice light field can strongly affect the timing of the seasonal vertical migration of zooplankton. These changes have the potential to impact on the future prosperity of ecological key species, their associated ecosystem functions, and biodiversity. This implies that considering biological processes during the twilight periods would be an important factor determining our ability to predict whether the CAO will become a ‘new oasis’ or a ‘desert’<sup>6</sup>, if the climate crisis cannot be controlled.

### Online content

Any methods, additional references, Nature Portfolio reporting summaries, source data, extended data, supplementary information, acknowledgements, peer review information; details of author contributions and competing interests; and statements of data and code availability are available at <https://doi.org/10.1038/s41558-023-01779-1>.

## References

1. Nicolaus, M., Katlein, C., Maslanik, J. & Hendricks, S. Changes in Arctic sea ice result in increasing light transmittance and absorption. *Geophys. Res. Lett.* **39**, L24501 (2012).
2. Sumata, H., de Steur, L., Divine, D. V., Granskog, M. A. & Gerland, S. Regime shift in Arctic Ocean sea ice thickness. *Nature* **615**, 443–449 (2023).
3. Notz, D. & Stroeve, J. The trajectory towards a seasonally ice-free Arctic Ocean. *Curr. Clim. Change Rep.* **4**, 407–416 (2018).
4. Wassmann, P. & Reigstad, M. Future Arctic Ocean seasonal ice zones and implications for pelagic–benthic coupling. *Oceanography* **24**, 220–231 (2011).
5. Tedesco, L., Vichi, M. & Scoccimarro, E. Sea-ice algal phenology in a warmer Arctic. *Sci. Adv.* **5**, eaav4830 (2019).
6. Ardyna, M. & Arrigo, K. R. Phytoplankton dynamics in a changing Arctic Ocean. *Nat. Clim. Change* **10**, 892–903 (2020).
7. Castellani, G. et al. Shine a light: under-ice light and its ecological implications in a changing Arctic Ocean. *Ambio* **51**, 307–317 (2022).
8. Brierley, A. S. Diel vertical migration. *Curr. Biol.* **24**, R1074–R1076 (2014).
9. Last Kim, S., Hobbs, L., Berge, J., Brierley Andrew, S. & Cottier, F. Moonlight drives ocean-scale mass vertical migration of zooplankton during the Arctic winter. *Curr. Biol.* **26**, 244–251 (2016).
10. Hobbs, L., Cottier, F. R., Las, K. S. & Berge, J. Pan-Arctic diel vertical migration during the polar night. *Mar. Ecol. Prog. Ser.* **605**, 61–72 (2018).
11. Geoffroy M. et al. Mesopelagic sound scattering layers of the high Arctic: seasonal variations in biomass, species assemblage, and trophic relationships. *Front. Mar. Sci.* **6** (2019).
12. Darnis G. et al. From polar night to midnight sun: diel vertical migration, metabolism and biogeochemical role of zooplankton in a high Arctic fjord (Kongsfjorden, Svalbard). *Limnol. Oceanogr.* **62**, 1586–1605 (2017).
13. Berge J. et al in: (eds) *Polar Night Marine Ecology: Life and Light in the Dead of Night* (eds Berge J., Johnsen G. & Cohen J. H.) 113–159 (Springer, 2020).
14. Jónasdóttir, S. H., Visser, A. W., Richardson, K. & Heath, M. R. Seasonal copepod lipid pump promotes carbon sequestration in the deep North Atlantic. *Proc. Natl Acad. Sci. USA* **112**, 12122–12126 (2015).
15. Darnis, G. & Fortier, L. Zooplankton respiration and the export of carbon at depth in the Amundsen Gulf (Arctic Ocean). *J. Geophys. Res. Oceans* **117**, C04013 (2012).
16. Visser, A. W., Grønning, J. & Jónasdóttir, S. H. *Calanus hyperboreus* and the lipid pump. *Limnol. Oceanogr.* **62**, 1155–1165 (2017).
17. Wilson, R. P. et al. Diel dive depth in penguins in relation to diel vertical migration of prey—whose dinner by candlelight. *Mar. Ecol. Prog. Ser.* **94**, 101–104 (1993).
18. Hays, G. C. A review of the adaptive significance and ecosystem consequences of zooplankton diel vertical migrations. *Hydrobiologia* **503**, 163–170 (2003).
19. Varpe, Ø., Daase, M. & Kristiansen, T. Food for thought: a fish-eye view on the new Arctic lightscape. *ICES J. Mar. Sci.* **72**, 2532–2538 (2015).
20. Gjosaeter H., Wiebe P. H., Knutsen T., Ingvaldsen R. B. Evidence of diel vertical migration of mesopelagic sound-scattering organisms in the Arctic. *Front. Mar. Sci.* **4** (2017).
21. Berge, J. et al. Artificial light during the polar night disrupts Arctic fish and zooplankton behaviour down to 200 m depth. *Commun. Biol.* **3**, 102 (2020).
22. Hobbs, L. et al. A marine zooplankton community vertically structured by light across diel to interannual timescales. *Biol. Lett.* **17**, 20200810 (2021).
23. Kohlbach, D. et al. The importance of ice algae-produced carbon in the central Arctic Ocean ecosystem: food web relationships revealed by lipid and stable isotope analyses. *Limnol. Oceanogr.* **61**, 2027–2044 (2016).
24. Kohlbach, D. et al. Dependency of Antarctic zooplankton species on ice algae-produced carbon suggests a sea ice-driven pelagic ecosystem during winter. *Glob. Change Biol.* **24**, 4667–4681 (2018).
25. Spitschan, M., Aguirre, G. K., Brainard, D. H. & Sweeney, A. M. Variation of outdoor illumination as a function of solar elevation and light pollution. *Sci. Rep.* **6**, 26756 (2016).
26. Rabe, B. et al. Overview of the MOSAiC expedition: physical oceanography. *Elem. Sci. Anth.* **10**, 000062 (2022).
27. Nicolaus, M. et al. Overview of the MOSAiC expedition: snow and sea ice. *Elem. Sci. Anth.* **10**, 000046 (2022).
28. Nicolaus, M., Hudson, S. R., Gerland, S. & Munderloh, K. A modern concept for autonomous and continuous measurements of spectral albedo and transmittance of sea ice. *Cold Reg. Sci. Technol.* **62**, 14–28 (2010).
29. Benoit-Bird, K. J. & Lawson, G. L. Ecological insights from pelagic habitats acquired using active acoustic techniques. *Annu. Rev. Mar. Sci.* **8**, 463–490 (2016).
30. Connan-McGinty, S. et al. Midnight sun to polar night: a model of seasonal light in the Barents Sea. *J. Adv. Model. Earth Syst.* **14**, e2022MS003198 (2022).
31. Skjoldal H. R. & Mundy P. *Large Marine Ecosystems (LMEs) of the Arctic Area Revision of the Arctic LME map*, 2 edn (Akureyri, 2013).
32. Clarke G. L. Light conditions in the sea in relation to the diurnal vertical migrations of animal. In Farquhar, G. B. (ed) *Proc. International Symposium on Biological Sound Scattering in the Ocean*, 41–50 (Maury Center Ocean Science, 1970).
33. Båtnes, A. S., Miljeteig, C., Berge, J., Greenacre, M. & Johnsen, G. Quantifying the light sensitivity of *Calanus* spp. during the polar night: potential for orchestrated migrations conducted by ambient light from the sun, moon, or aurora borealis? *Polar Biol.* **38**, 51–65 (2015).
34. Geynrikh A., Kosobokova K., Rudyakov Y. A. Seasonal variations in the vertical distribution of some prolific copepods of the Arctic Basin. *Can. Translations Fish. Aquat. Sci.* **4925** (1983).
35. Hirche, H.-J. & Mumm, N. Distribution of dominant copepods in the Nansen Basin, Arctic Ocean, in summer. *Deep Sea Res. A* **39**, S485–S505 (1992).
36. Kvile, K. Ø., Ashjian, C. & Ji, R. Pan-Arctic depth distribution of diapausing *Calanus* copepods. *Biol. Bull.* **237**, 76–89 (2019).
37. Gradinger, R., Meiners, K., Plumley, G., Zhang, Q. & Bluhm, B. A. Abundance and composition of the sea-ice meiofauna in off-shore pack ice of the Beaufort Gyre in summer 2002 and 2003. *Polar Biol.* **28**, 171–181 (2005).
38. Hardge, K. et al. The importance of sea ice for exchange of habitat-specific protist communities in the Central Arctic Ocean. *J. Mar. Syst.* **165**, 124–138 (2017).
39. Ehrlich, J. et al. Sea-ice associated carbon flux in Arctic spring. *Elem. Sci. Anth.* **9**, 00169 (2021).
40. Kunisch E. H. et al. What we do in the dark: prevalence of omnivorous feeding activity in Arctic zooplankton during polar night. *Limnol. Oceanogr.* (2023).
41. Koch, C. W. et al. Year-round utilization of sea ice-associated carbon in Arctic ecosystems. *Nat. Commun.* **14**, 1964 (2023).
42. Hobbs L., Banas N. S., Cottier F. R., Berge J. & Daase M. Eat or sleep: availability of winter prey explains mid-winter and spring activity in an Arctic *Calanus* population. *Front. Mar. Sci.*, **7** (2020).
43. Kohlbach D. et al. Winter carnivory and diapause counteract the reliance on ice algae by Barents Sea zooplankton. *Front. Mar. Sci.* **266** (2021).



44. Ross, T. & Lavery, A. C. Acoustic scattering from density and sound speed gradients: modeling of oceanic pycnoclines. *J. Acoust. Soc. Am.* **131**, EL54–EL60 (2012).
45. Notz, D. & SIMIP Community. Arctic sea ice in CMIP6. *Geophys. Res. Lett.* **47**, e2019GL086749 (2020).
46. Wassmann, P. Arctic marine ecosystems in an era of rapid climate change. *Prog. Oceanogr.* **90**, 1–17 (2011).
47. Leu, E., Soreide, J. E., Hessen, D. O., Falk-Petersen, S. & Berge, J. Consequences of changing sea-ice cover for primary and secondary producers in the European Arctic shelf seas: timing, quantity, and quality. *Prog. Oceanogr.* **90**, 18–32 (2011).
48. Hirche, H.-J. & Niehoff, B. Reproduction of the Arctic copepod *Calanus hyperboreus* in the Greenland Sea—field and laboratory observations. *Polar Biol.* **16**, 209–219 (1996).
49. Ershova, E. A. et al. Sea ice decline drives biogeographical shifts of key *Calanus* species in the Central Arctic Ocean. *Glob. Change Biol.* **27**, 2128–2143 (2021).
50. Darnis, G., Wold, A., Falk-Petersen, S., Graeve, M. & Fortier, L. Could offspring predation offset the successful reproduction of the arctic copepod *Calanus hyperboreus* under reduced sea-ice cover conditions? *Prog. Oceanogr.* **170**, 107–118 (2019).
51. Gradinger, R. R. & Bluhm, B. A. In-situ observations on the distribution and behavior of amphipods and Arctic cod (*Boreogadus saida*) under the sea ice of the High Arctic Canada Basin. *Polar Biol.* **27**, 595–603 (2004).
52. Kohlbach, D. et al. Strong linkage of polar cod (*Boreogadus saida*) to sea ice algae-produced carbon: evidence from stomach content, fatty acid and stable isotope analyses. *Prog. Oceanogr.* **152**, 62–74 (2017).
53. Geoffroy, M. et al. The circumpolar impacts of climate change and anthropogenic stressors on Arctic cod (*Boreogadus saida*) and its ecosystem. *Elem. Sci. Anth.* **11** (2023).
54. Snoeijs-Leijonmalm, P. et al. Unexpected fish and squid in the central Arctic deep scattering layer. *Sci. Adv.* **8**, eabj7536 (2022).
55. Jakobsson, M. et al. The International Bathymetric Chart of the Arctic Ocean version 4.0. *Sci. Data* **7**, 176 (2020).
56. Soreide, J. E., Leu, E., Berge, J., Graeve, M. & Falk-Petersen, S. Timing of blooms, algal food quality and *Calanus glacialis* reproduction and growth in a changing Arctic. *Glob. Change Biol.* **16**, 3154–3163 (2010).

**Publisher's note** Springer Nature remains neutral with regard to jurisdictional claims in published maps and institutional affiliations.

**Open Access** This article is licensed under a Creative Commons Attribution 4.0 International License, which permits use, sharing, adaptation, distribution and reproduction in any medium or format, as long as you give appropriate credit to the original author(s) and the source, provide a link to the Creative Commons license, and indicate if changes were made. The images or other third party material in this article are included in the article's Creative Commons license, unless indicated otherwise in a credit line to the material. If material is not included in the article's Creative Commons license and your intended use is not permitted by statutory regulation or exceeds the permitted use, you will need to obtain permission directly from the copyright holder. To view a copy of this license, visit <http://creativecommons.org/licenses/by/4.0/>.

© The Author(s) 2023

## Methods

### Autonomous biophysical observatory

We deployed an autonomous biophysical observatory on the ice floe of the MOSAiC expedition of RV *Polarstern* in September 2020 (PS122/5). This observatory made it possible to investigate the distribution of zooplankton in the top 50 m under the drifting sea ice in relation to environmental parameters, without introducing disturbance by invasive sampling gear or artificial light. The main component was an AZFP buoy (ASL Environmental Sciences) which recorded zooplankton vertical distribution from the autumn–winter transition close to the geographic North Pole on 18 September 2020 to the winter–spring transition north of Greenland on 1 April 2021. These measurements were complemented by under-ice irradiance and oceanographic measurements obtained from several co-deployed platforms.

**AZFP buoy.** The AZFP was integrated into a rugged sea-ice tethered buoy designed to survive the harsh conditions of the ice-covered ocean by Brunco Observation Systems. The surface unit of the buoy was composed of a heavy metal cylinder housing the batteries, a solid frame carrying the main electronics, a glass half-dome with solar panels and a stable floatation body around the main hull. The buoy was powered by alkaline batteries sufficient for several months of operation, complemented by a solar-rechargeable power supply to support a higher sampling interval during summer. The surface unit was equipped with additional sensors, including GPS position, under-ice fluorescence, temperature, salinity and cameras. The underwater unit mainly consisted of the AZFP with its four downward-looking acoustic transducers, mounted in a frame fixed to the bottom of the battery cylinder with multiple steel wires and hanging just beneath the ice base (Extended Data Fig. 1). The buoy ran on a Linux operating system, configured to poll the entire sensor suite at regular intervals, and to transmit the recordings to a land-based station via the Iridium satellite network. AZFP sampling parameters and measurement intervals could be adjusted via a remote satellite connection at any time. The buoy was installed on the MOSAiC ice floe on 12 September 2020, in a hydro-hole through 1.3-m-thick level ice.

The AZFP recorded acoustic backscatter of zooplankton and fish in the water column at four frequencies: 67, 125, 200 and 455 kHz. In this study, we present data from the 125, 200 and 455 kHz transducers. The manufacturer calibrated all frequencies of the AZFP before deployment ( $\pm 1$  dB re  $1 \text{ m}^{-1}$ ). The transducers had a nominal  $-3$  dB beam angle of  $10^\circ$  at 67 kHz,  $8^\circ$  at 125 and 200 kHz and  $7^\circ$  at 455 kHz. The pulse length was set to 500  $\mu\text{s}$ , and the ping rate was 0.5 Hz in all frequencies. Measurements were averaged over burst periods of 2 min and a vertical cell height of about 0.5 m.

The AZFP buoy was fully operational on 18 September 2020. The last data transmission was recorded on 7 May 2021. For the purpose of this study, we limited the data to the period from the start of the twilight period at the end of the polar day on 18 September 2020 ( $89.1^\circ \text{ N } 107.4^\circ \text{ E}$ ) to the end of the twilight period at the end of the polar night on 1 April 2021 ( $84.6^\circ \text{ N } 22.3^\circ \text{ W}$ ). During this period, the observatory was mainly drifting over the Arctic Basin.

To maintain sufficient battery power, we applied an adaptive interval scheme. At the start of the survey on 18 September 2020, AZFP measurements were conducted every 2 h for a period of 20 min (10 bursts), and for 10 min (5 bursts) after 30 September 2020 (Supplementary Table 1). To save battery power during darkness, the interval between measurements was set to 12 h between 19 and 29 October 2020, and the measurement duration was increased to 20 min on 20 October 2020 (Supplementary Table 1). After 29 October 2020, the interval between measurements was set to 3 h, and the duration of measurements was reduced to 6 min (3 bursts). To maintain sufficient battery power until the end of the winter, the interval between measurements was further increased to 4 h on 12 January 2021 (Supplementary Table 1). The hydroacoustic data of the AZFP buoy are available at <https://doi.org/10.1594/PANGAEA.954939> ref. 57.

**Hydroacoustic data processing.** Acoustic data were processed with Echoview 12 (Echoview Software). We used Echoview's built-in algorithm to remove background and impulse noise, applying a minimum signal-to-noise ratio of 10 (refs. 58,59). In addition, echograms were visually inspected for bad data regions and artefacts, which were manually removed. Data were expressed as volume backscattering strength ( $S_v$  in dB re  $1 \text{ m}^{-1}$ ) for each measurement cell ( $\sim 0.5 \text{ m} \times 2 \text{ min}$ ) between 1 m below the ice and 50 m depth. Initial data exploration revealed the presence of a pronounced SBM between about 20 and 30 m depth, which persisted from the beginning of the measurements until mid-March 2021 (Fig. 1). This SBM corresponded to a strong difference in salinity between CTD sensors positioned above and below the SBM and a strong density gradient (Supplementary Fig. 1), indicating that the elevated backscatter could have been related to both the impedance by a pycnocline and the aggregation of zooplankton at the pycnocline (Extended Data Fig. 3)<sup>44</sup>. The overlap of potential zooplankton backscatter with pycnocline-related backscatter did not compromise observations of the relative shifts in the vertical distribution of scatterers. For the analysis of DVM in the twilight periods (Fig. 2a,b and Extended Data Fig. 2), we integrated the backscatter data in 2-min-long cells reaching from 1 m depth to approximately 2 m above the SBM. For each integration cell, we calculated the nautical area scattering coefficient ( $s_n$  in  $\text{m}^2 \text{ nmi}^{-2}$ ). A multifrequency analysis was conducted to discriminate the acoustic signal from different functional zooplankton groups based on their acoustic frequency response<sup>42</sup>. In short, the  $S_v$  echograms were divided into 2-min-long by 1-m-deep cells before being compared. Cells where  $S_{v125\text{kHz}} < S_{v200\text{kHz}} < S_{v455\text{kHz}}$  were assigned to copepods, cells where  $S_{v125\text{kHz}} > S_{v200\text{kHz}} < S_{v455\text{kHz}}$  were assumed to be dominated by larger zooplankton such as euphausiids or amphipods, and cells where  $S_{v125\text{kHz}} < S_{v200\text{kHz}} > S_{v455\text{kHz}}$  were assigned to chaetognaths. Data analysis and graphical presentation was conducted in R v.3.6.1 (ref. 60), using the editor RStudio v.2023.06.0 (ref. 61) as a programming tool.

**Radiation station.** A spectral radiation station consisting of three spectral radiometers (RAMSES-ACC-VIS, TriOS) was installed  $\sim 50$  m from the AZFP buoy on 27 August 2020. The upward-looking under-ice sensor was installed 0.5 m below the ice base of a refrozen melt pond to measure transmitted irradiance. The sensor also carried an inclination and pressure module. A second upward-looking sensor was installed above the surface to measure incident irradiance as a reference. An external tiltmeter was attached to the sensor. The station also carried a third downward-looking radiometer measuring reflected irradiance, a light chain to measure in-ice light attenuation, a snow pinger to measure snow accumulation and a camera to monitor the state of the observatory (not used here). The radiation station stopped operating on 13 November 2020. The radiation station data are available at <https://doi.org/10.1594/PANGAEA.948838> ref. 62.

**CTD buoy.** Water column structure was recorded and transmitted via the Iridium satellite network by a buoy equipped with five SBE37IMP Microcat CTDs (Sea-Bird Scientific) at 10, 20, 50, 75 and 100 m depth along an inductive modem tether. The buoy itself was built by Pacific Gyre. It was deployed at a location  $\sim 120$  m from the AZFP buoy on 28 August 2020. The transmission interval was set to 10 min. A more detailed description of the buoy is given in Hoppmann et al.<sup>63</sup>. The data of this buoy are available online at <https://doi.org/10.1594/PANGAEA.954992> ref. 64.

### Zooplankton sampling

On 16 September 2020 at station PS122/5\_62-71 of the MOSAiC expedition, the epipelagic zooplankton community was sampled vertically from 50 m depth to the surface (Hydrobios Multinet Midi; 150  $\mu\text{m}$  mesh size,  $0.25 \text{ m}^2$ ). The multinet was equipped with an electronic flow meter measuring the amount of filtered water in  $\text{m}^3$  for each sample. Immediately after sampling, the animals were preserved in a

4% formaldehyde–seawater solution buffered with hexamethylenetetramine, and stored at room temperature until quantitative analysis at the Alfred-Wegener-Institute using the ZooScan scanning system<sup>65</sup> (Biotom, Hydroptic). The sample was size-fractionated by sieving over 70 µm, 500 µm and 1,000 µm meshes to avoid overlapping large and small organisms on the scanner. The three size fractions were then scanned with a resolution of 2,400 d.p.i. The resulting scan was processed and separated into images with single objects using ZooProcess v.7.29 (ref. 65), a macro applied in ImageJ v.1.41o (ref. 66). The length and width of each individual (major axis, minor axis) were automatically measured. The single object images were uploaded to EcoTaxa<sup>67</sup>, a web application for the semiautomatic taxonomic classification of the images and sorted into taxonomic categories. Assuming each object to be an ellipsoid, the volume (mm<sup>3</sup>) of each zooplankton individual was calculated using the formula:

$$V = \frac{4\pi}{3} \times \frac{a}{2} \times \left(\frac{b}{2}\right)^2 \quad (1)$$

where  $V$  is the volume of an organism,  $a$  is the major axis and  $b$  is the minor axis. The biovolume of each taxonomic category was then calculated as the sum of all such individual volumes divided by the amount of filtered water of each sample (mm<sup>3</sup> m<sup>-3</sup>).

### Modelling under-ice light and projecting shift of DVM onset

**Calculation of light intensity triggering vertical migration.** To estimate the level of light intensity triggering the autumn DVM of zooplankton into the under-ice habitat above the SBM, we first identified the date on which the DVM crossed the SBM. To this end, we calculated the mean  $S_v$  within the under-ice habitat for each measurement interval between 20 September and 15 October 2020 (Supplementary Fig. 3). This figure reveals a very clear transition between low mean scattering values (around -90 dB) to higher mean scattering values (between -85 dB and -80 dB). This transition occurred between consecutive AZFP readings at 12:14:18 and 15:56:47 (UTC) on 28 September 2020. Then, we used the measured under-ice irradiance data from the radiation station and propagated it into the water column using an exponential decay following:

$$I_w = I_{ui} \times \exp(-k_w \times d_z) \quad (2)$$

where  $I_w$  is the light intensity in W m<sup>-2</sup> transmitted into the water column,  $I_{ui}$  is the under-ice light intensity measured by the radiation buoy,  $k_w$  is the water attenuation coefficient and  $d_z$  is the incremental depth in metres.

We calculated the attenuation in the water ( $k_w$ ) from spectral light measurements (400–700 nm) conducted by a remotely operated vehicle<sup>68</sup> during seven dives in March and September 2020 ( $n = 1,213$  measurements)<sup>69</sup>. The mean  $k_w$  over the first 25 m depth was estimated at  $0.14 \pm 0.01$  m<sup>-1</sup> (mean  $\pm$  s.d.). We provide the trigger level as irradiance (W m<sup>-2</sup>) and a photosynthetic photon flux density (PPFD, µmol photons m<sup>-2</sup> s<sup>-1</sup>). For the irradiance, we considered the visible part of the spectrum (400–700 nm) from the measurements. For the PPFD, the trigger level was first estimated in W m<sup>-2</sup> considering the total spectrum available (320–950 nm), and then converted into µmol photons m<sup>-2</sup> s<sup>-1</sup> following Castellani et al.<sup>70</sup>. The resulting irradiance light level at the depth of the SBM when DVM began (25 m) was  $2.4 \times 10^{-4}$  W m<sup>-2</sup>. Based on the standard deviation of  $k_w$ , this value was associated with an uncertainty of  $\pm 0.65 \times 10^{-4}$  W m<sup>-2</sup>. The corresponding PPFD value was  $6.2 \times 10^{-4}$  µmol photons m<sup>-2</sup> s<sup>-1</sup>, with an uncertainty of  $1.6 \times 10^{-4}$  µmol photons m<sup>-2</sup> s<sup>-1</sup>. In addition, we provide the light threshold for two single wavelengths in the blue part of the spectrum (455 nm) and the green part of the spectrum (530 nm) to compare our results with previous studies. The light thresholds for 455 and 530 nm were  $7.06 \times 10^{-6}$  and  $2.28 \times 10^{-6}$  µmol photons m<sup>-2</sup> s<sup>-1</sup>, respectively. We

then plotted the evolution of this trigger isolume and its uncertainty range as a function of time and depth with the backscatter data (Fig. 2c).

The trigger isolume rose through the SBM on 28 September and continued to become shallower in depth until it fully reached the surface on 7 October 2020. To statistically confirm the visual impression that the upper limit of high zooplankton backscatter followed the evolution of this trigger isolume during this period (Fig. 2c), we performed a one-sided paired  $t$ -test testing the null hypothesis that, within each measurement interval, mean  $S_v$  values above the trigger isolume were not significantly lower than below it. Mean  $S_v$  values above and below the trigger isolume between 28 September and 7 October 2020 were calculated by first transforming  $S_v$  values into their linear form  $s_v$  to compute mean  $s_v$  within each measurement interval, and then transforming the mean  $s_v$  back into its logarithmic form  $S_v$ . Paired  $t$ -tests for all three analysed frequencies showed that mean  $S_v$  was significantly lower above the trigger isolume than below it throughout the period of DVM (125 kHz:  $t = -29.707$ , d.f. = 586,  $P < 0.001$ ; 200 kHz:  $t = -32.095$ , d.f. = 585,  $P < 0.001$ ; 455 kHz:  $t = -24.485$ , d.f. = 586,  $P < 0.001$ ). This confirmed the notion that most zooplankton scatterers stayed below the trigger isolume and followed its daily up and down motion within the under-ice habitat.

**Modelling.** As a proxy of the expected mid-21st-century shift in the onset of the autumn and spring DVM, we calculated the difference (in days) between the mean dates when the trigger isolume reaches 25 m depth in both seasons for the 10 yr period 2015–2024 and for the 2045–2054 period. The projected shifts were determined considering future sea-ice concentration, sea-ice thickness, snow depth, cloud area fraction and surface temperature. To achieve this, we used model outputs based on the scenarios SSP1-2.6 and SSP5-8.5 from four different IPCC CMIP6 model ensembles. The model experiments used in this study have shown a reasonable climate-change-driven sea-ice loss compared to the change in global mean temperature<sup>45</sup>. Further selection criteria were the availability of daily outputs and of multiple ensemble members. The models were (number of ensemble members in parentheses): ACCESS-CM2 (5)<sup>71</sup>, MPI-ESM1-2-HR (2)<sup>72</sup>, MPI-ESM1-2-LR (29)<sup>73</sup> and MRI-ESM2-0 (5)<sup>74</sup>. Decadal means for the periods 2015–2024 and 2045–2054 were calculated for sea-ice concentration, sea-ice thickness, snow depth, cloud area fraction and surface temperature for each ensemble member for the autumn–winter transition (September–December) and for the winter–spring transition (January to March). All ensemble members of each of the model scenario experiments were used to accommodate internal model variability (Supplementary Figs. 4–7).

Downwelling shortwave radiation at the surface was taken from the Clouds and the Earth's Radiant Energy System (CERES) synoptic satellite-based products<sup>75</sup>. These products were available daily, at a  $1^\circ \times 1^\circ$  resolution over the Arctic Ocean and from instruments on board the Terra and Aqua satellites. Because future downwelling radiation is unknown, and our investigation focuses on the relative effect of future sea-ice and snow conditions predicted by climate model experiments, we used observed downwelling radiation for the period 1 September to 20 December 2020 and 1 January to 31 March 2021 for all years. As twilight and night light levels of downwelling shortwave radiation are not provided by this remote sensing dataset, we used twilight downwelling irradiance estimates based on the Commission Internationale de l'Éclairage (CIE) daylight model, extended with implemented supplementary basic functions based on field measurements, with corrections for solar angles<sup>25,30</sup>. For the purpose of this study, we calculated incoming solar spectra for sun angles between  $-28^\circ$  and  $0^\circ$  at a  $2^\circ$  resolution. The broadband albedo was calculated based on observations during the SHEBA ice-drift experiment and considered constant at 0.84 (ref. 76).

The light transmission through snow and sea ice was calculated using an exponential decay of light through snow and sea ice using



varying extinction coefficients based on physical conditions<sup>7</sup>. With this approach, snow depth and sea-ice thickness subgrid scale distributions are applied to account for the variability within each grid cell. For the water column, we applied the extinction coefficient determined during the MOSAiC expedition ( $K_w = 0.14 \text{ m}^{-1}$ ). Then, we calculated the depth profiles of transmitted light into the water column in each grid cell of the 25 km EASE grid, averaged for the 2015–2024 and the 2045–2054 decades, respectively. These datasets were used to determine the Julian day at which the trigger level of  $2.4 \times 10^{-4} \text{ W m}^{-2}$  ( $6.2 \times 10^{-4} \mu\text{mol photons m}^{-2} \text{ s}^{-1}$ ) is reached at a depth of 25 m in autumn and spring. The average ensemble values, standard deviations, minimum and maximum for each model in the different Arctic LMEs<sup>31</sup> displayed in Table 1 and Supplementary Tables 2 and 3 were estimated using the Arctic mask shown in Supplementary Fig. 2. All calculations and analyses performed in the section Modeling under-ice light and projecting shift of DVM onset were performed in Python 3.7.13 and MATLAB\_R2021.

### Reporting summary

Further information on research design is available in the Nature Portfolio Reporting Summary linked to this article.

### Data availability

AZFP data are available at <https://doi.org/10.1594/PANGAEA.954939> (ref. 57). CTD buoy data are available at <https://doi.org/10.1594/PANGAEA.954992> (ref. 64). Spectral light data are available at <https://doi.org/10.1594/PANGAEA.948838> (ref. 62) and <https://doi.org/10.1594/PANGAEA.935688> (ref. 69).

### Code availability

Code for analysing AZFP and zooplankton data, including related datasets, is available at <https://doi.org/10.5281/zenodo.8100957> (ref. 57). Code for the multifrequency analysis of AZFP data, including related datasets, is available at <https://doi.org/10.5281/zenodo.8124371> (ref. 77). Code for calculating a trigger isolume for zooplankton vertical migration and calculating shifts in vertical migration onset based on CMIP6 model outputs is available at <https://doi.org/10.5281/zenodo.8130995> (ref. 78).

### References

57. Flores H. et al. Hydroacoustic backscatter recorded by buoy 2020AZFP1 in the central Arctic Ocean during Sep 2020–May 2021. *PANGAEA* <https://doi.org/10.1594/PANGAEA.954939> (2023).
58. De Robertis, A. & Higginbottom, I. A post-processing technique to estimate the signal-to-noise ratio and remove echosounder background noise. *ICES J. Mar. Sci.* **64**, 1282–1291 (2007).
59. Ryan, T. E., Downie, R. A., Kloser, R. J. & Keith, G. Reducing bias due to noise and attenuation in open-ocean echo integration data. *ICES J. Mar. Sci.* **72**, 2482–2493 (2015).
60. R Development Core Team. *R: A Language and Environment for Statistical Computing* (R Foundation for Statistical Computing, 2019).
61. RStudio\_Team. RStudio: Integrated Development for R. Ver.:2023.06.0. (RStudio, 2023); <http://www.rstudio.com/>
62. Nicolaus M., Hoppmann M., Tao R. & Katlein C. Spectral radiation fluxes, albedo and transmittance from autonomous measurement from Radiation Station 2020R21, deployed during MOSAiC 2019/20. *PANGAEA* <https://doi.org/10.1594/PANGAEA.948838> (in review).
63. Hoppmann, M., Kuznetsov, I., Fang, Y. C. & Rabe, B. Mesoscale observations of temperature and salinity in the Arctic Transpolar Drift: a high-resolution dataset from the MOSAiC Distributed Network. *Earth Syst. Sci. Data* **14**, 4901–4921 (2022).
64. Hoppmann M. et al. Raw data files recorded by CTD buoy 2020O10 in the Arctic Transpolar Drift in 2020/21 as part of the MOSAiC Leg 5 (PS122/5) buoy deployments. *PANGAEA* <https://doi.org/10.1594/PANGAEA.954992> (2023).

65. Gorsky, G. et al. Digital zooplankton image analysis using the ZooScan integrated system. *J. Plankton Res.* **32**, 285–303 (2010).
66. Schneider, C. A., Rasband, W. S. & Eliceiri, K. W. NIH Image to ImageJ: 25 years of image analysis. *Nat. Methods* **9**, 671–675 (2012).
67. Picheral M., Colin S. & Irisson J. O. EcoTaxa—a tool for the taxonomic classification of images (2017) <http://ecotaxa.obs-vlfr.fr/>
68. Katlein C. et al. A new remotely operated sensor platform for interdisciplinary observations under sea ice. *Front. Mar. Sci.* **4** (2017).
69. Nicolaus M. et al. Spectral solar radiation over and under sea ice during the MOSAiC campaign 2019/20. *PANGAEA* <https://doi.org/10.1594/PANGAEA.935688> (2021).
70. Castellani, G., Losch, M., Lange, B. A. & Flores, H. Modeling Arctic sea-ice algae: physical drivers of spatial distribution and algae phenology. *J. Geophys Res-Oceans* **122**, 7466–7487 (2017).
71. Dix, M. et al. CSIRO-ARCCSS ACCESS-CM2 model output prepared for CMIP6 CMIP. *Earth Syst. Grid Federation* <https://doi.org/10.22033/ESGF/CMIP6.2281> (2019).
72. Jungclaus, J. et al. MPI-M MPIESM1.2-HR model output prepared for CMIP6 CMIP. *Earth Syst. Grid Federation* <https://doi.org/10.22033/ESGF/CMIP6.741> (2019).
73. Brovkin, V. et al. MPI-M MPIESM1.2-LR model output prepared for CMIP6 C4MIP. *Earth Syst. Grid Federation* <https://doi.org/10.22033/ESGF/CMIP6.748> (2019).
74. Yukimoto, S. et al. MRI MRI-ESM2.0 model output prepared for CMIP6 AerChemMIP. *Earth Syst. Grid Federation* <https://doi.org/10.22033/ESGF/CMIP6.633> (2019).
75. Rutan, D. A. et al. CERES synoptic product: methodology and validation of surface radiant flux. *J. Atmos. Ocean. Technol.* **32**, 1121–1143 (2015).
76. Perovich, D., Grenfell, T., Light, B., Richter-Menge, J. & Tucker, T. Wavelength-integrated albedos, v1.0 (UCAR/NCAR, 2007).
77. Priou, P., Geoffroy, M. & Flores, H. MOSAiC—AZFP multifrequency analysis, v1. (Zenodo, 2023); <https://doi.org/10.5281/zenodo.8124371>
78. Veysière, G., Karcher, M., Flores, H., Wilkinson, J. & Stroeve, J. Analysis of future predictions of pan-Arctic under-ice light and subsequent zooplankton vertical migration shift in the water column, v1 (Zenodo, 2023); <https://doi.org/10.5281/zenodo.8130995>

### Acknowledgements

We thank the MOSAiC science crew of the teams ECO, OCEAN and ICE, and the captain and crew of RV *Polarstern* for their support during MOSAiC PS122/5 (grant number AWI\_PS122\_00). We are particularly grateful to Z. Koenig, J. Allerholt, S. Karam, M. Gallagher, Z. Brasseur and J. Regnery for their help with the field deployments. We thank J.-H. Kim, the captain, crew and science crew of RV *Araon* cruise ARA10B for their support in a preliminary study without which the autonomous AZFP buoy would not have been possible. We thank S. Krägefsky (AWI) and A. Atkinson (PLM) for their advice. N. Knüppel (AWI) supported the zooplankton analysis. This study was primarily funded by the project EcoLight, as part of the bilateral Changing Arctic Ocean programme by the British National Environmental Research Council (NERC) under grant number NE/R012725/1 and the German Ministry for Education and Research (BMBF) under grant number O3V01465 and O3F0811A and B. A.C. was funded through BMBF grant O3F0917A, MOSAiC 3. G.C., H.F. and B.N. were also funded by the Helmholtz Association's Programme Oriented Funding Period 4 (POF-4), Topic and 6.1 and 6.3. K.S. was funded through NERC Grant NE/S002502/1. M.G. and P.P. were financially supported by the Ocean Frontier Institute of the Canada First Research Excellence Fund, Natural Sciences and Engineering Research Council Discovery Grant programme, ArcticNet a Network of Centres of Excellence Canada, Research Council of Norway grant 300333 Deep Impact, and Fisheries and Oceans Canada

through the Atlantic Fisheries Fund. M.K.'s work described in this paper has been partially funded from the European Union's Horizon 2020 research and innovation programme through the project Arctic PASSION under grant agreement number 101003472. The instruments and buoy developments were funded by the Frontiers in Arctic Marine Monitoring (FRAM) and the Multidisciplinary Ice-based Distributed Observatory (MIDO) infrastructure programmes.

### Author contributions

G.C., H.F., M.H., M.K., J.S., G.V. and J.W. conceived the research and designed the study. G.C., H.F., M.H., L.V. and J.W. developed the autonomous AZFP buoy. M.G. and P.P. advised on hydroacoustic sampling and data analysis. G.C., M.H., M.N. and K.S. performed the field work during MOSAiC. A.C., H.F., M.H., M.K., B.N., G.V. and J.W. analysed the data. H.F. and G.V. drafted the manuscript. All authors participated in writing the paper, discussed, interpreted results and drew conclusions.

### Funding

Open access funding provided by Alfred-Wegener-Institut.

### Competing interests

The authors declare no competing interests.

### Additional information

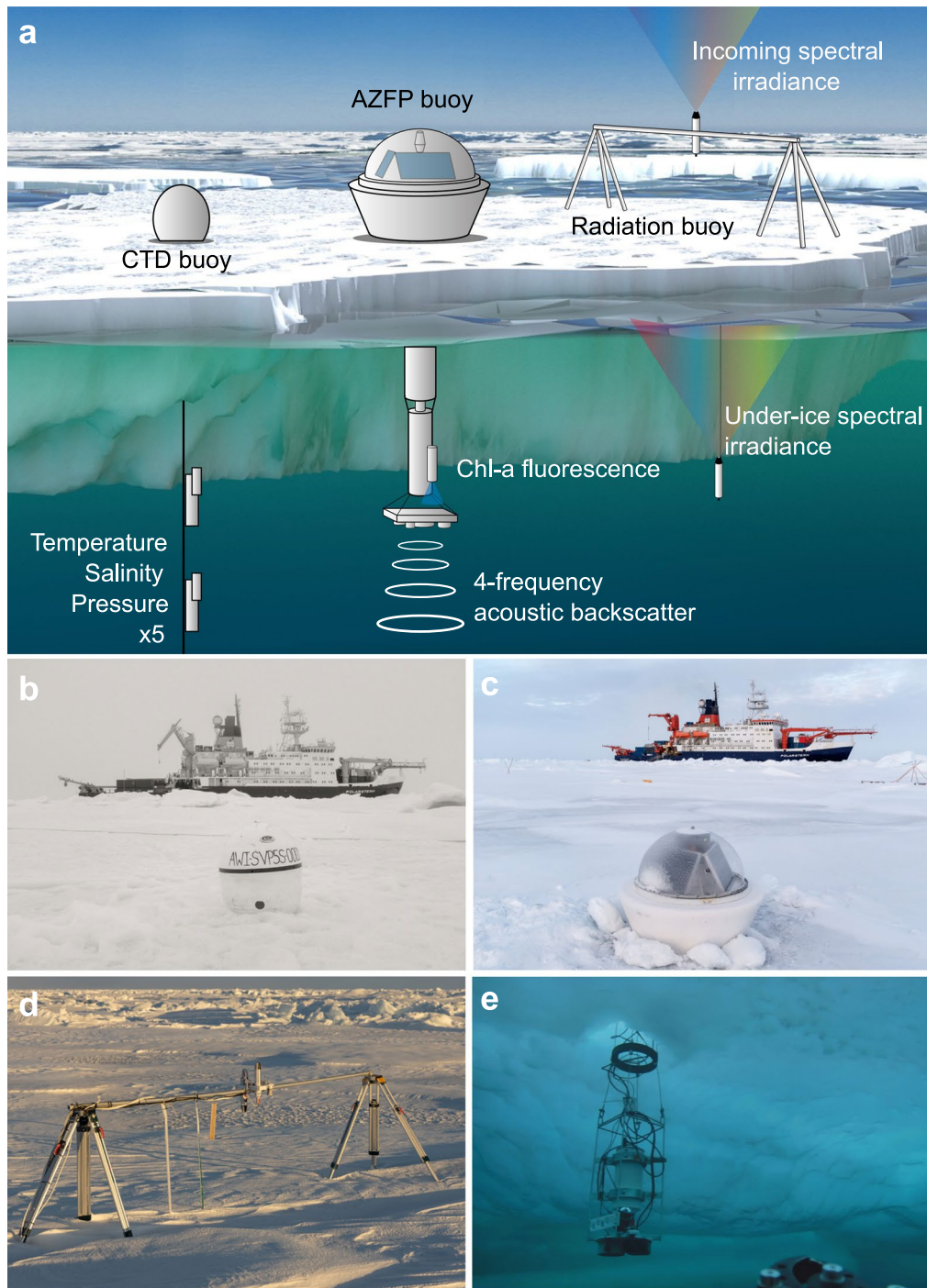
**Extended data** is available for this paper at <https://doi.org/10.1038/s41558-023-01779-1>.

**Supplementary information** The online version contains supplementary material available at <https://doi.org/10.1038/s41558-023-01779-1>.

**Correspondence and requests for materials** should be addressed to Hauke Flores.

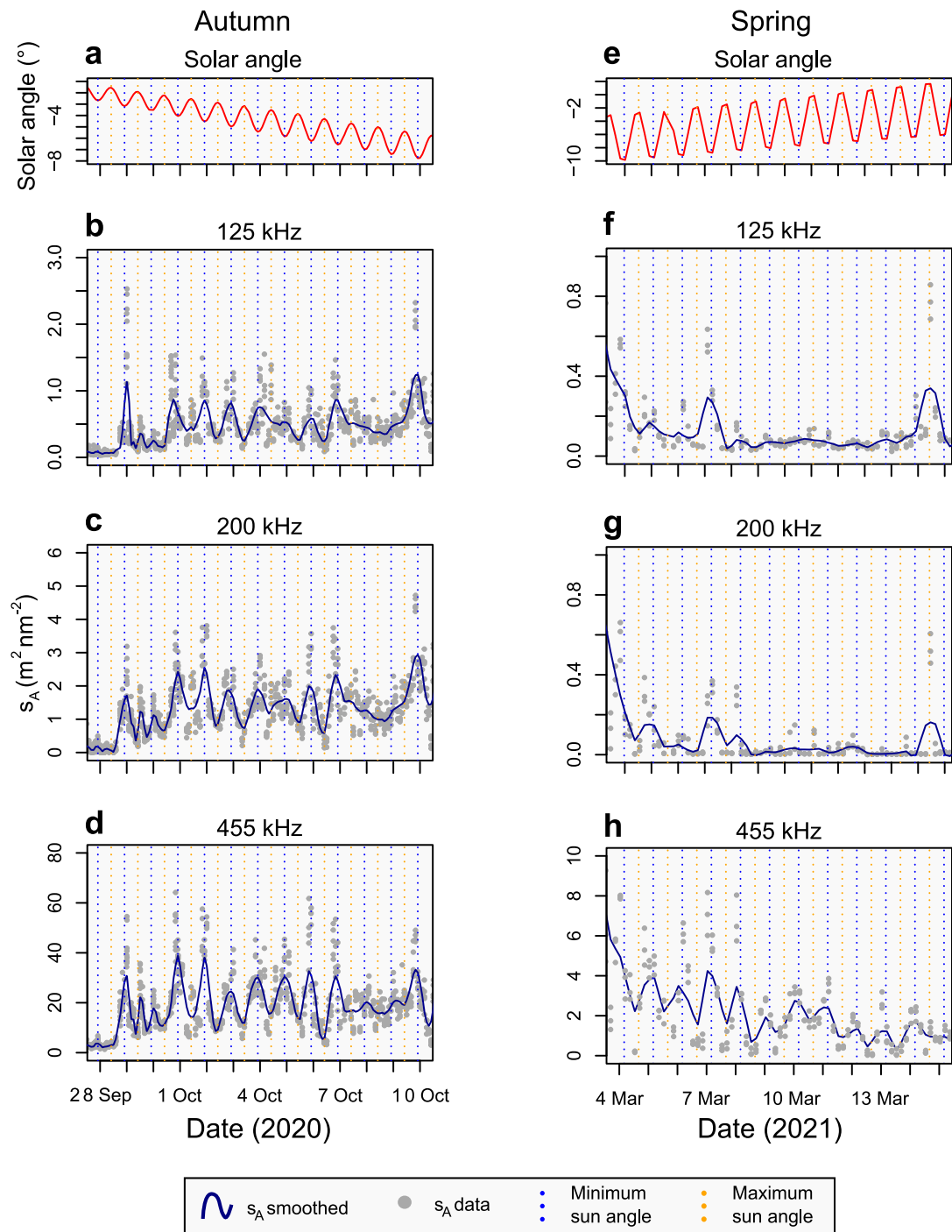
**Peer review information** *Nature Climate Change* thanks Jonathan Cohen, Letizia Tedesco, Atsushi Yamaguchi and the other, anonymous, reviewer(s) for their contribution to the peer review of this work.

**Reprints and permissions information** is available at [www.nature.com/reprints](http://www.nature.com/reprints).



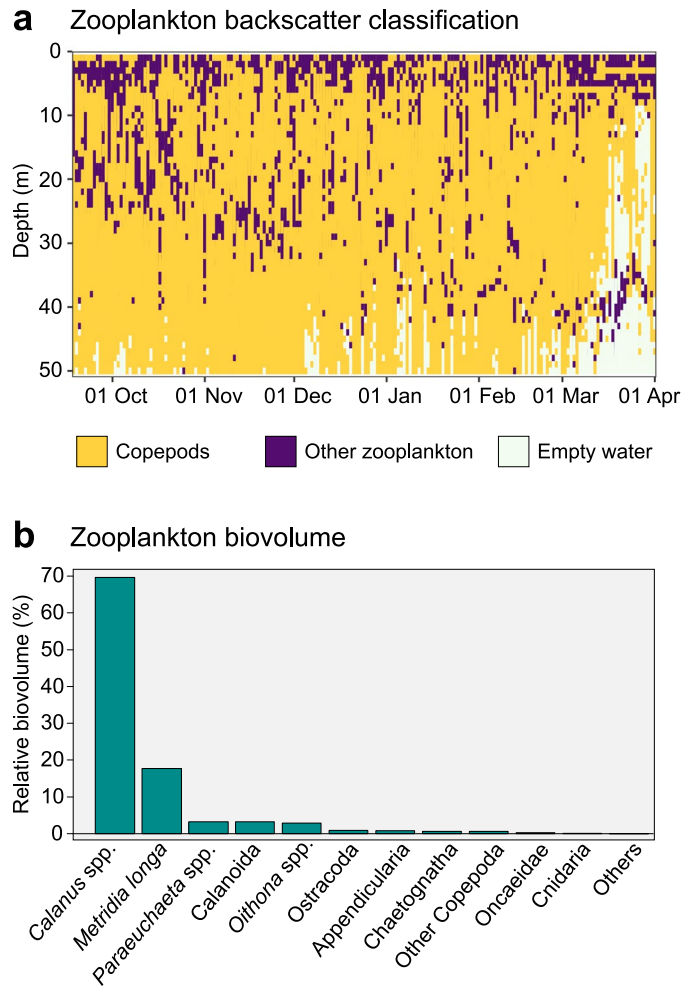
**Extended Data Fig. 1 | Autonomous bio-physical sea-ice observatory. a**, Schematic of drifting observatory; **b**, CTD buoy surface unit; **c**, AZFP buoy surface unit; **d**, Radiation station; **e**, AZFP buoy underwater package photographed by a remotely operated vehicle.





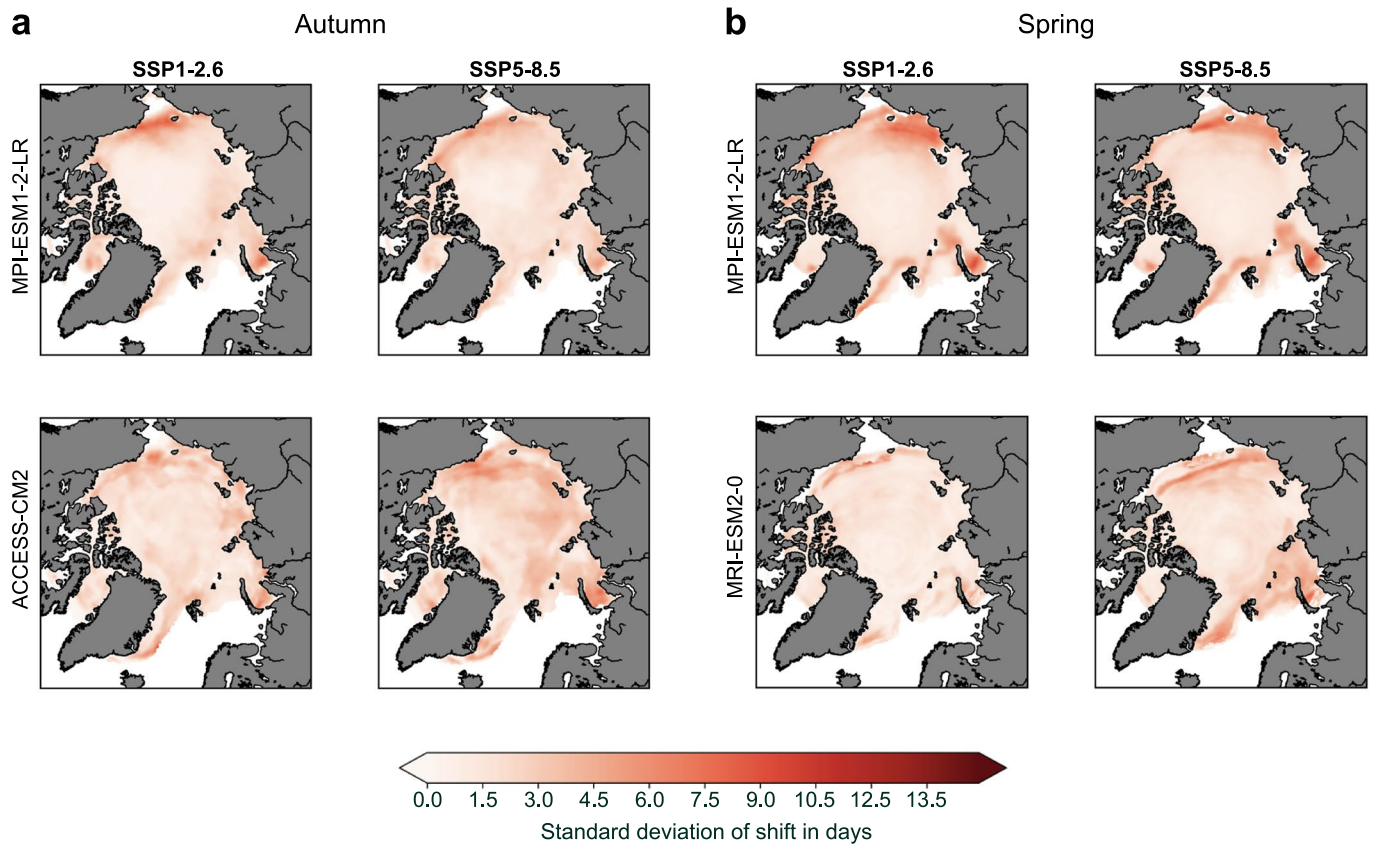
**Extended Data Fig. 2 | Diel variability of depth-integrated backscatter during the autumn and spring twilight periods.** Solar angle and nautical area scattering coefficient ( $s_A$ ,  $\text{m}^2 \text{nm}^{-2}$ ) at 125, 200 and 455 kHz above the surface

backscatter maximum during the autumn (a-d) and spring (e-h) twilight periods. Dark blue lines indicate the relative change in  $s_A$  during the day estimated by a loess smoother.



**Extended Data Fig. 3 | Taxonomic composition of zooplankton in the 0-50 m surface layer.** **a**, Vertical distribution of the different functional groups of zooplankton based on multifrequency analysis according to Darnis et al.<sup>12</sup>. Copepods dominated the acoustic signal in 83% of the cells and larger zooplankton, such as euphausiids and amphipods, dominated in 15% of the cells.

The multifrequency analysis indicates aggregation of larger zooplankton at the Subsurface Backscatter Maximum (SBM), but this assignment by the algorithm may be an artefact from the strong density gradient. **b**, Relative biovolume of zooplankton taxa in the top 50 m sampled with a multinet at station PS122/5\_62-71 on 16 September 2020.



**Extended Data Fig. 4 | Variability of potential projected future shift in diel vertical migration (DVM) onset.** Pan-Arctic maps of the standard deviation of the potential mean shift of the autumn (a) and spring (b) DVM onset for SSP1-2.6

and SSP5-8.5, over all ensemble members of the models projecting the most extreme shifts shown in Figs. 3 and 4, when contrasting 2045–2054 with the baseline in 2015–2024.



## Reporting Summary

Nature Portfolio wishes to improve the reproducibility of the work that we publish. This form provides structure for consistency and transparency in reporting. For further information on Nature Portfolio policies, see our [Editorial Policies](#) and the [Editorial Policy Checklist](#).

### Statistics

For all statistical analyses, confirm that the following items are present in the figure legend, table legend, main text, or Methods section.

| n/a                                 | Confirmed  |
|-------------------------------------|--|
| <input checked="" type="checkbox"/> | <input type="checkbox"/> The exact sample size ( $n$ ) for each experimental group/condition, given as a discrete number and unit of measurement   |
| <input checked="" type="checkbox"/> | <input type="checkbox"/> A statement on whether measurements were taken from distinct samples or whether the same sample was measured repeatedly   |
| <input type="checkbox"/>            | <input checked="" type="checkbox"/> The statistical test(s) used AND whether they are one- or two-sided<br><i>Only common tests should be described solely by name; describe more complex techniques in the Methods section.</i>   |
| <input checked="" type="checkbox"/> | <input type="checkbox"/> A description of all covariates tested  |
| <input checked="" type="checkbox"/> | <input type="checkbox"/> A description of any assumptions or corrections, such as tests of normality and adjustment for multiple comparisons   |
| <input type="checkbox"/>            | <input checked="" type="checkbox"/> A full description of the statistical parameters including central tendency (e.g. means) or other basic estimates (e.g. regression coefficient) AND variation (e.g. standard deviation) or associated estimates of uncertainty (e.g. confidence intervals) |
| <input type="checkbox"/>            | <input checked="" type="checkbox"/> For null hypothesis testing, the test statistic (e.g. $F$ , $t$ , $r$ ) with confidence intervals, effect sizes, degrees of freedom and $P$ value noted<br><i>Give <math>P</math> values as exact values whenever suitable.</i>                            |
| <input checked="" type="checkbox"/> | <input type="checkbox"/> For Bayesian analysis, information on the choice of priors and Markov chain Monte Carlo settings  |
| <input checked="" type="checkbox"/> | <input type="checkbox"/> For hierarchical and complex designs, identification of the appropriate level for tests and full reporting of outcomes  |
| <input checked="" type="checkbox"/> | <input type="checkbox"/> Estimates of effect sizes (e.g. Cohen's $d$ , Pearson's $r$ ), indicating how they were calculated  |

*Our web collection on [statistics for biologists](#) contains articles on many of the points above.*

### Software and code

Policy information about [availability of computer code](#)

|                 |  |
|-----------------|--|
| Data collection | Data was collected with a self-programmed autonomous observatory. All code involved in data collection was written by our co-author Lovro Valcic   |
| Data analysis   | Hydroacoustic data were retrieved and cleaned in the commercial software Echoview 12. They were analysed in R (Version 3.6.1), using RStudio Version 2023.06.0 as a programming tool. Light data and model projections were performed in Python version 3.7.13 and the commercial software package MATLAB_R2021. All code for data processing are published at Zenodo: Flores, Hauke, Veyssière, Gaëlle, Wilkinson, Jeremy, Cornils, Astrid. Analysis of AZFP data from a multidisciplinary drift observatory in the Central Arctic Ocean. (Version 1). ZENODO <a href="https://doi.org/10.5281/zenodo.8100957">https://doi.org/10.5281/zenodo.8100957</a> (2023). Priou, Pierre, Geoffroy, Maxime, Flores, Hauke. MOSAiC - AZFP multifrequency analysis. ZENODO <a href="https://doi.org/10.5281/zenodo.8124371">https://doi.org/10.5281/zenodo.8124371</a> (2023). Veyssière, Gaëlle, Karcher, Michael, Flores, Hauke, Wilkinson, Jeremy & Stroeve, Julienne. Analysis of future predictions of pan-Arctic under-ice light and subsequent zooplankton vertical migration shift in the water column (Version 1). ZENODO <a href="https://doi.org/10.5281/zenodo.8130995">https://doi.org/10.5281/zenodo.8130995</a> (2023). |

For manuscripts utilizing custom algorithms or software that are central to the research but not yet described in published literature, software must be made available to editors and reviewers. We strongly encourage code deposition in a community repository (e.g. GitHub). See the Nature Portfolio [guidelines for submitting code & software](#) for further information.

## Data

Policy information about [availability of data](#)

All manuscripts must include a [data availability statement](#). This statement should provide the following information, where applicable:

- Accession codes, unique identifiers, or web links for publicly available datasets
- A description of any restrictions on data availability
- For clinical datasets or third party data, please ensure that the statement adheres to our [policy](#)

AZFP data are available at: Flores, Hauke, Castellani, Giulia, Wilkinson, Jeremy, Valcic, Lovro, Hoppmann, Mario, Veysiere, Gaelle, Karcher, Michael J, Nicolaus, Marcel, Stroeve, Julienne C (2023): Hydroacoustic backscatter recorded by buoy 2020AZFP1 in the central Arctic Ocean during Sep 2020 - May 2021. <https://doi.org/10.1594/PANGAEA.954939>. CTD buoy data are available at: Hoppmann, Mario, Kuznetsov, Ivan, Fang, Ying-Chih, Rabe, Benjamin, Karam, Salar, Allerholt, Jacob, Koenig, Zoé, Jónsson, Jón Ásgeir, Macrander, Andreas (2023): Raw data files recorded by CTD buoy 2020O10 in the Arctic Transpolar Drift in 2020/21 as part of the MOSAiC Leg 5 (PS122/5) buoy deployments. <https://doi.org/10.1594/PANGAEA.954992>. Spectral light data are available at: Nicolaus, Marcel, Hoppmann, Mario, Tao, Ran, Katlein, Christian (2022): Spectral radiation fluxes, albedo and transmittance from autonomous measurement from Radiation Station 2020R21, deployed during MOSAiC 2019/20. <https://doi.org/10.1594/PANGAEA.948838> and: Nicolaus, Marcel, Anhaus, Philipp, Arndt, Stefanie, Katlein, Christian, Krampe, Daniela, Lange, Benjamin Allen, Matero, Ilkka, Regnery, Julia, Rohde, Jan, Schiller, Martin (2021): Spectral solar radiation over and under sea ice during the MOSAiC campaign 2019/20. <https://doi.org/10.1594/PANGAEA.935688>

## Human research participants

Policy information about [studies involving human research participants and Sex and Gender in Research](#).

Reporting on sex and gender

N/A

Population characteristics

N/A

Recruitment

N/A

Ethics oversight

N/A

Note that full information on the approval of the study protocol must also be provided in the manuscript.

## Field-specific reporting

Please select the one below that is the best fit for your research. If you are not sure, read the appropriate sections before making your selection.

- Life sciences  Behavioural & social sciences  Ecological, evolutionary & environmental sciences

For a reference copy of the document with all sections, see [nature.com/documents/nr-reporting-summary-flat.pdf](https://www.nature.com/documents/nr-reporting-summary-flat.pdf)

## Ecological, evolutionary & environmental sciences study design

All studies must disclose on these points even when the disclosure is negative.

Study description

We used an ice-tethered drifting autonomous bio-physical observatory to study the distribution of scatterers (zooplankton), light and other environmental parameters in the 50 m under sea ice of the Central Arctic Ocean. From the combination of hydroacoustic backscatter data and light we estimated a level of light intensity that triggers the vertical migration of zooplankton. We applied this trigger level to CMIP6 model scenarios to project the shift of the timing of zooplankton vertical migration in the future, when sea ice will be thinner and more light will enter the Arctic Ocean.

Research sample

We sampled hydroacoustic backscatter strength at 3 frequencies representing mesozooplankton: 125, 200 and 455 kHz.

Sampling strategy

We analyzed the full dataset and did not subsample.

Data collection

The data were collected automatically by our autonomous observatory, while it drifted across the Central Arctic Ocean

Timing and spatial scale

We analysed data collected during the period from 18 September 2020 to 1 April 2021. The sampling frequency and intervals were provided in the Online Methods section: To maintain sufficient battery power, we applied an adaptive interval scheme. At the start of the survey on 18 September 2020, AZFP measurements were conducted every 2 hours for a period of 20 minutes (10 bursts), and for 10 minutes (5 bursts) after 30 September 2020 (Supplementary Table 2). To save battery power during darkness, the interval between measurements was set to 12 hours between 19 and 29 October 2020, and the measurement duration was increased to 20 minutes on 20 October 2020 (Supplementary Table 1). After 29 October 2020, the interval between measurements was set to 3 hours, and the duration of measurements was reduced to 6 minutes (3 bursts). To maintain sufficient battery power until the end of the winter, the interval between measurements was further increased to 4 hours on 12 January 2021 (Supplementary Table 1).

|                                   |   |
|-----------------------------------|---|
| Data exclusions                   | We excluded data collected before 18 September 2020 due to multiple disturbances caused by activities on the MOSAiC ice floe, and after 1 April 2021 because the polar day had begun, and this study focuses on the polar night including the adjacent twilight periods. We reported the presence of data in the 67 kHz frequency in the manuscript, but did not present results from this frequency because the very low backscatter strength in this frequency impeded a meaningful analysis. |
| Reproducibility                   | The part of this study presenting newly collected data is not an experiment, but based on measurements in the environment. The measurements can be reproduced in the exact same way with the information given in the manuscript, but the results may differ. We provide all information necessary to reproduce model projections with our published datasets.  |
| Randomization                     | We conducted a one-sided paired t-test to test the null hypothesis that backscatter above the vertical migration trigger isolume was not significantly lower than below it. For this test, we included all backscatter data from the relevant twilight period between 2020/09/28 and 2020/10/07 between 50 depth and the surface. The test was performed separately for the frequencies 125, 200 and 455 kHz. No data were subsampled or excluded.  |
| Blinding                          | Blinding was not necessary in this study, as it presents only environmental data.   |
| Did the study involve field work? | <input checked="" type="checkbox"/> Yes <input type="checkbox"/> No   |

## Field work, collection and transport

|                        |  |
|------------------------|--|
| Field conditions       | The observatory was deployed on the MOSAiC leg 5 ice floe in the Central Arctic Ocean. The air temperature was below the freezing point during the entire study period. Water temperatures ranged between 0°C and -1.9°C, depending on depth and location.   |
| Location               | The observatory was deployed at 89.1°N 107.4°E and the last data point considered in this study was at 84.6°N 22.3°W. For details see Supplementary Table 1 and Figure 1.  |
| Access & import/export | The observatory was deployed during the MOSAiC study of RV Polarstern (PS122/5). No national permits were needed as the work took entirely place in the Arctic High Seas. MOSAiC did however acquire research permits for the waters around Greenland and Svalbard to ensure data collection in the Exclusive Economic Zones of Norway and Greenland (Denmark), if the MOSAiC floe or any measurement device drifted into these areas.   |
| Disturbance            | Potential disturbance was limited to the period of the deployment of the observatory on 12 September 2020 and lasted less than 24 hours. The area impacted during this time was less than 25 m <sup>2</sup> . After deployment, our observatory did not impact on the environment anymore. The only emissions were the weak hydroacoustic pulses used to detect zooplankton. The power was lower than in comparable echosounders used on commercial and research vessels and are not known to harm fish or endotherms. |

## Reporting for specific materials, systems and methods

We require information from authors about some types of materials, experimental systems and methods used in many studies. Here, indicate whether each material, system or method listed is relevant to your study. If you are not sure if a list item applies to your research, read the appropriate section before selecting a response.

### Materials & experimental systems

| n/a                                 | Included in the study                                  |
|-------------------------------------|--|
| <input checked="" type="checkbox"/> | <input type="checkbox"/> Antibodies                    |
| <input checked="" type="checkbox"/> | <input type="checkbox"/> Eukaryotic cell lines         |
| <input checked="" type="checkbox"/> | <input type="checkbox"/> Palaeontology and archaeology |
| <input checked="" type="checkbox"/> | <input type="checkbox"/> Animals and other organisms   |
| <input checked="" type="checkbox"/> | <input type="checkbox"/> Clinical data                 |
| <input checked="" type="checkbox"/> | <input type="checkbox"/> Dual use research of concern  |

### Methods

| n/a                                 | Included in the study                           |
|-------------------------------------|---|
| <input checked="" type="checkbox"/> | <input type="checkbox"/> ChIP-seq               |
| <input checked="" type="checkbox"/> | <input type="checkbox"/> Flow cytometry         |
| <input checked="" type="checkbox"/> | <input type="checkbox"/> MRI-based neuroimaging |